Enhancing Clinical Support for Breast Cancer with Deep Learning Models using Optimized Synthetic Correlated Diffusion Imaging

by

Chi-en Amy Tai

A thesis
presented to the University of Waterloo
in fulfillment of the
thesis requirement for the degree of
Master of Applied Science
in
Systems Design Engineering

Waterloo, Ontario, Canada, 2024

Author's Declaration

This thesis consists of material all of which I authored or co-authored: see Statement of Contributions included in the thesis. This is a true copy of the thesis, including any required final revisions, as accepted by my examiners.

I understand that my thesis may be made electronically available to the public.

Statement of Contributions

The following papers are used in this thesis. I was the primary author with major contributions to the design, development, analysis, writing, and editing of the papers.

- **C. A. Tai**, H. Gunraj, and A. Wong, "A Multi-Institutional Open-Source Benchmark Dataset for Breast Cancer Clinical Decision Support using Synthetic Correlated Diffusion Imaging Data", *Conference on Computer Vision and Pattern Recognition (CVPR) Women in Computer Vision (WiCV)*, 2023. [1]

  This paper is incorporated in Chapter 3. H. Gunraj helped obtain the source data and A. Wong reviewed and provided feedback for the paper. I performed the synthetic correlated diffusion computation from the source data, created the multiparametric MRI creation, analyzed the dataset, and wrote the entire paper.

- **C. A. Tai**, H. Gunraj, N. Hodzic, N. Flanagan, A. Sabri, and A. Wong, "Enhancing Clinical Support for Breast Cancer with Deep Learning Models Using Synthetic Correlated Diffusion Imaging", *International Workshop on Applications of Medical AI. Cham: Springer Nature Switzerland*, 2023. [2]

  This paper is incorporated in Chapter 4 and Chapter 5. H. Gunraj helped obtain the source data and edit the paper. N. Hodzic and N. Flanagan conducted initial examination on machine learning models. A. Sabri reviewed the data and paper. A. Sabri provided clinical interpretation of the images and gave feedback on the paper. A. Wong reviewed and provided feedback for the paper. I conducted initial examination on deep learning models, implemented and performed all the experiments included in the paper, and wrote the entire paper.

Abstract

Breast cancer is the second most common type of cancer in women in Canada and the United States, representing over 25% of all new female cancer cases. The prevalence of breast cancer continues to grow, affecting about 300,000 females in the United States in 2023. However, there are different levels of severity of breast cancer requiring different treatment strategies, and hence, grading breast cancer and estimating treatment prognosis have become vital clinical tasks in breast cancer.

Recently, a new form of magnetic resonance imaging (MRI) called synthetic correlated diffusion imaging (CDI^s) imaging was introduced to address the physical hardware limitations and showed considerable promise for clinical decision support for cancers such as prostate cancer when compared to current gold-standard MRI techniques. However, the efficacy for CDI^s for other forms of cancers such as breast cancer has not been as well-explored.

This thesis explores and designs novel deep learning architectures for enhancing two breast cancer clinical task performance (pathologic complete response prediction and Scarff-Bloom-Richardson grade classification) with optimized CDI^s. A volumetric convolutional neural network is leveraged to learn volumetric deep radiomic features from a pre-treatment cohort, constructing a predictor based on the learned features for grade and post-treatment response prediction. The optimization of parameters for computing CDI^s for breast cancer is also conducted through improving tumour delineation.

The proposed approach was evaluated using the ACRIN-6698 study and compared against current gold-standard MRI modalities. For grade prediction, using optimized CDI^s achieved a leave-one-out cross-validation accuracy of 95.79%, which is over 16% above the next best gold-standard MRI modality and over 6% above using the unoptimized CDI^s. Additionally, using optimized CDI^s for post-treatment response prediction resulted in a leave-one-out cross-validation accuracy of 93.28%, which is over 8.5% above the next best gold-standard MRI modality and over 5.5% above using the unoptimized CDI^s.

The proposed approach demonstrates how using optimized CDI^s can be used to enhance the performance of breast cancer clinical tasks, indicating its potential as a valuable tool for oncologists to enhance patient treatment within the breast cancer domain and beyond.

Acknowledgements

I would like to thank my amazing supervisor Professor Alexander Wong for all the support and mentorship over the past two years. It has been a phenomenal experience learning from you and you have inspired me to pursue opportunities that I never would have considered before. You are truly a wonderful *research dad* and I will forever be grateful that you accepted me into your lab.

I would also like to thank Professor David Clausi and Professor Lukasz Golab for reviewing my thesis. I really appreciate this as I see how insanely busy you are.

Furthermore, thank you to Professor David Clausi and Professor Yuhao Chen, along with all the fabulous people at the Vision and Image Processing Lab for the support, smiles, laughs and giggles throughout my master's. I will fondly remember our fun adventures and board game nights. Special thank you to Hayden Gunraj for onboarding me to medical imaging and being a solid emotional support/unfiltered tangent-fun buddy.

In addition, I would like to thank Professor Lukasz Golab again for inspiring me during my undergraduate program to pursue this field and his energetically contagious energy during his courses. It was an absolute pleasure being a part of your class and doing a URA with you. I never would have imagined pursuing a Master's without your motivation and kindness. Sincere thank you also to Professor Ada Hurst, Professor Brian Cozzarin, Professor Mark Smucker, Professor Anwar Hasan, and Crystal Roma for the encouragement, experiences, motivational talks, and opportunities in undergrad, and my high school teachers Mr. Zuber, Mr. Bannon, Mr. Pigeon, and Ms. Schuck for the academic foundation.

I would be remiss not to mention my amazing coworkers and managers from Microsoft, Brian, James, Ben, Steve, Tina, Scott, and Murali for supporting me and allowing me to pursue opportunities I never thought possible. You all have been absolutely incredible. I would also like to thank Justin, Brian, Kristina, and Caitlin from my first internship at Pepsi for helping me build a solid foundation for my career and confidence in the workplace.

Special thank you to my friends and family who have been my emotional support throughout my entire life and although the list is long, I would especially like to thank my best friend Aly, my high school friends Pam, Logan, Kiersten, Lela, Gabriel, and Stephanie, my undergraduate close friends Bradley, Seher, and Sara, my grad school support network Emily, Nicholas, Krzysztof, Alex, Chyrine, Robbie, Owen and Gautam, and my entire varsity squash team with special mention to Ahmed, Nitya, Khaaliqa, and Jillian. Thank you for believing in me, even during the bumps in the road and always being there for me.

Finally, I would like to thank the Natural Sciences and Engineering Research Council of Canada and the University of Waterloo for funding this research.

Dedication

This is dedicated to my family for supporting me throughout my entire life journey and inspiring me to believe that nothing is impossible.

My mom for effortlessly balancing three jobs, courses and taking care of children.

My dad for successfully getting a PhD while working and spending time with family.

My brother for never giving up on his dreams and showing me hard work pays off.

My sister for being fearless and a full-time babysitter during our childhood and beyond.

I truly would not be where I am without y'all.

Table of Contents

List of Figures

List of Tables

List of Abbreviations

ACRIN American College of Radiology Imaging Network

ADC apparent diffusion coefficient

AUC area under the receiver operating characteristic curve

BCa breast cancer

CDI correlated diffusion imaging

CDI^{s} synthetic correlated diffusion imaging

CT computed tomography

DCE dynamic contrast-enhanced imaging

DWI diffusion-weighted imaging

DWI b = 800 diffusion-weighted imaging for the b-value of 800

LOOCV leave-one-out cross-validation

MONAI Medical Open Network for AI

mpMRI^{cdis}

MRI magnetic resonance imaging

MRLD longest diameter on the MRI

PCa prostate cancer

pCR pathologic complete response

ResNet Residual Network

SBR Scarff-Bloom-Richardson

T0 pre-treatment

T2w T2-weighted

Chapter 1

Introduction

Breast cancer is the second most common type of cancer in females in Canada and the United States, representing over 25% of all new female cancer cases [3]. As such, there has been immense research and progress on improving screening techniques and processes to proactively detect the presence of breast cancer in individuals at risk [4]. However, it is estimated that 2,261,419 new cases of breast cancer were diagnosed across the world in 2020 [3] and predicted that 43,700 American women will die from breast cancer in 2023 [5].

1.1 Breast Cancer Screening and Diagnosis

While breast cancer can indeed be a serious condition, it is crucial to understand that not all cases are fatal, with some being more severe than others. When patients are first diagnosed with breast cancer, they are categorized into two main types: in situ and invasive breast cancer [5]. In situ is a less severe form of breast cancer that is a precursor to invasive breast cancer. The latter type, invasive breast cancer, represents approximately 80% of diagnosed cases and signifies that the cancer has already or can spread into the nearby tissue areas [5, 3].

For breast cancer clinical support tasks, pathologists typically consult the patient's magnetic resonance imaging (MRI) images. Current gold-standard MRI modalities include diffusion-weighted imaging (DWI), apparent diffusion coefficient (ADC), and T2-weighted (T2w) [6]. DWI is a form of MRI that measures the motion of water molecules within the tissue with the b values (0, 100, 600, 800) denoting the specific configuration of the scanner such as gradient strength with 0 indicating no diffusion sensitivity and a greater sensitivity

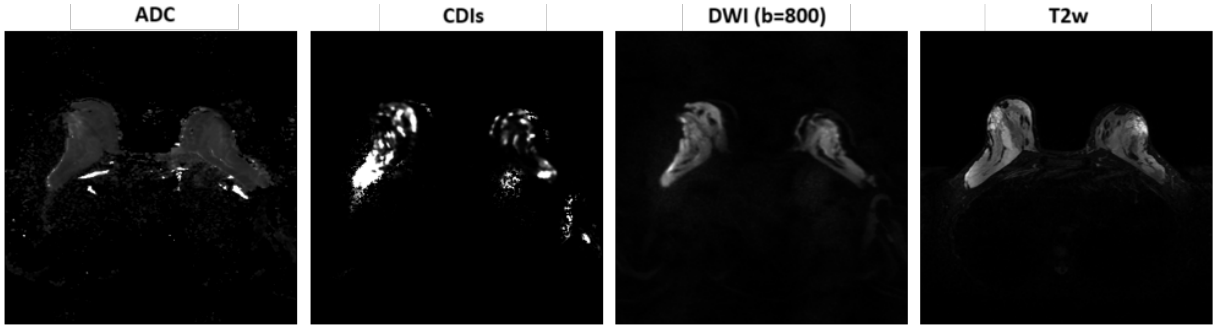

Figure 1.1: Example slice illustrating visual differences between ADC, CDI^s, DWI, and T2w at pre-treatment for a patient who has SBR Grade II (Intermediate).

as b increases [7]. ADC is the value obtained by taking the slope of the curve created with the different b values with lower ADC indicating regions with restricted diffusion or potentially cancerous tissue [8]. T2w is a type of contrast MRI image that enhances water signals [9]. Recently, synthetic correlated diffusion imaging (CDI^s) was introduced as a promising imaging modality for clinical decision support for prostate cancer [10]. CDI^s introduces synthetic signals by extrapolating MRI data to introduce more data points by analyzing the direction of diffusion in the cancerous tissue. An illustrative example highlighting the visual differences between the imaging modalities of ADC, CDI^s, DWI (b=800), and T2w for a patient case is shown Figure 1.1.

Patients with invasive breast cancer also often receive a breast cancer grade that represents the similarity of the cancer cells to normal cells under the microscope [11, 12, 13]. The three breast cancer grades (low, intermediate, and high) describe the speed of growth and likelihood of a good prognosis [14, 15, 11]. Low grade (grade 1) cancer has the best prognosis with slow growth and spread of the cancer, while high grade (grade 3) cancer has the worst prognosis with the greatest difference between cancer and normal cells and represent cancer that is fast-growing with quick spread to other cells. As such, the stage and grade of breast cancer are vital factors used to determine the severity of breast cancer and discern the best treatment strategy as the stage and grade have been shown to relate to the success of various treatment strategies [16].

1.2 Scarff-Bloom-Richardson Grade Classification

Specifically, the gold-standard Scarff-Bloom-Richardson (SBR) grade (with example CDI^s shown in Figure 1.2) has been shown to consistently indicate a patient's response to chemotherapy [17].

Unfortunately, the gold-standard method of grading the breast cancer is currently determined by a pathologist looking at a tissue sample from the cancer tumour under a microscope. As such, the current method to determine the grade requires removal of some cancer cells from the patient which can lead to stress and discomfort along with high medical costs [5].

Previous studies have examined the merit of pairing computer vision techniques for breast cancer grade prediction using radiomics [18], statistical tests [8], elasticity ratios [19], multitask learning models [20], and deep learning [21]. A comprehensive review of radiomics discussed the high potential of tumor grade prediction using radiomics on breast imaging [18] and Burnside et al. [22] demonstrated that computer-extracted image phenotypes on MRI could accurately predict the breast cancer stage. However, Surov et al. concluded that diffusion-weighted imaging used with the Mann-Whitney U test was inapt at predicting breast cancer tumour grades [8]. On the other hand, deep learning methods to identify metastatic breast cancer [4] and breast cancer grade [21] have presented high accuracies of over 80% with a review on invasive breast cancer supporting the importance of leveraging artificial intelligence on grade prediction [16].

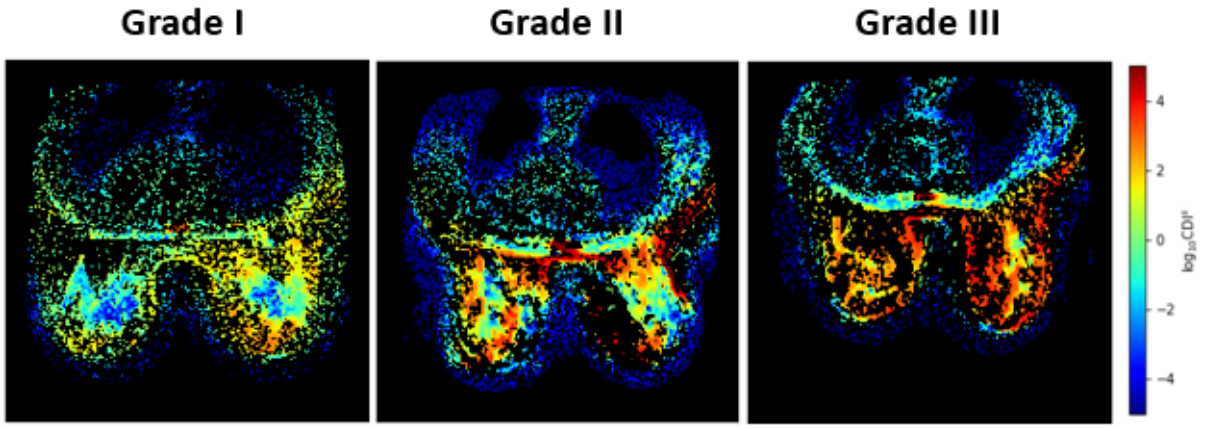

Figure 1.2: Example breast CDI^s images for the different SBR grades.

1.3 Pathologic Complete Response Prediction

Following grading, surgery is commonly administered to prevent breast cancer from further developing and to remove cancerous tissue [5]. However, some non-metastatic breast cancer tumors are inoperable [23]. Recently, a type of treatment termed neoadjuvant chemotherapy has risen in usage as it can shrink a large tumor before surgery (so that the tumor can become operable) [23] and it may also result in a pathologic complete response (pCR) which is the absence of active cancer cells present in surgery [24]. Example breast CDI^s images with and without pCR is shown in Figure 1.3. However, neoadjuvant chemotherapy is expensive, time-consuming, and may expose patients to radiation as well as lead to other significant side effects such as reduced fertility [25].

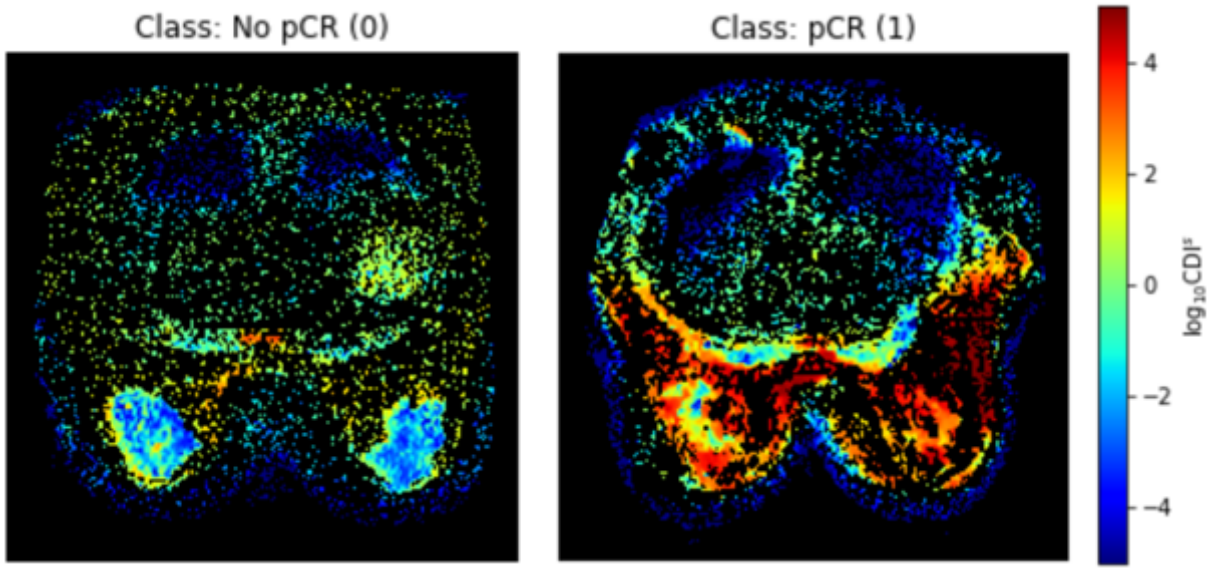

Figure 1.3: Example breast CDI^s images with and without pCR.

The current process to recommend neoadjuvant chemotherapy is based on the expert judgment of the medical oncologist and/or radiation oncologist of whether the patient will live longer and benefit from the treatment [26]. With potential biases and high uncertainty in human clinical judgment [27], there is potential for some erroneous recommendations leading to some patients later developing preventable detrimental advanced cancer or being exposed to unnecessary radiation.

In the past, a variety of different modalities and methods were investigated to predict pathologic complete response with patient features such as using a nonparametric Mann-Whitney test for DWI and MRS [28], logistic regression models on MRI images [29], hard threshold parameter values [30], AdaBoost classifier with qCT features [31], and an assortment of machine learning models with qCT features [32]. Furthermore, previous studies have also examined the usage of deep learning and volumetric data with breast cancer. Convolutional neural network algorithms were studied to predict post-NAC axillary response with breast MRI images [33], a three-layer 3D CNN architecture was trained to detect breast cancer using a dataset of 5547 images with an AUC of 0.85 [34], and convolutional neural networks with 3D MRI images were used to predict pCR to neoadjuvant chemotherapy in breast cancer [35].

1.4 Thesis Contributions

This thesis explores and designs novel deep learning architectures for enhancing the performance for two breast cancer clinical tasks (pathologic complete response prediction and Scarff-Bloom-Richardson grade classification) employing a newly introduced MRI modality called CDI^s. It also examines the optimization of parameters for computing CDI^s specifically for breast cancer to further enhance task performance. A volumetric convolutional neural network is leveraged to learn volumetric deep radiomic features from a pre-treatment cohort, constructing a predictor based on the learned features for SBR grade and pCR prediction. Subsequently, there are two main contributions:

1. **Dataset**: The computation and optimization of exponents used to generate CDI^s for breast cancer. The process to create the dataset is described in Chapter 3.
2. **Workflow**: The proposed workflow for learning volumetric deep radiomic features from a pre-treatment cohort, with a predictor for SBR grade and pCR prediction (shown in Figure 1.4). The setup, results, and analysis for pCR prediction and SBR grade classification are described in Chapter 4 and Chapter 5, respectively.

In this thesis, a review of relevant background concepts is provided in Chapter 2. The description of the computation of CDI^s images for the patients is detailed in Chapter 3. Problem formulation, experimental setup, experimental results, and summary using the proposed workflow for pCR prediction and SBR grade are described in Chapter 4 and Chapter 5 respectively. Optimizing CDI^s for breast cancer tumour delineation is described

in Chapter 6 and clinical support enhancement for breast cancer with optimized CDI^s is presented in Chapter 7. Finally, conclusions, limitations, and future work are discussed in Chapter 8.

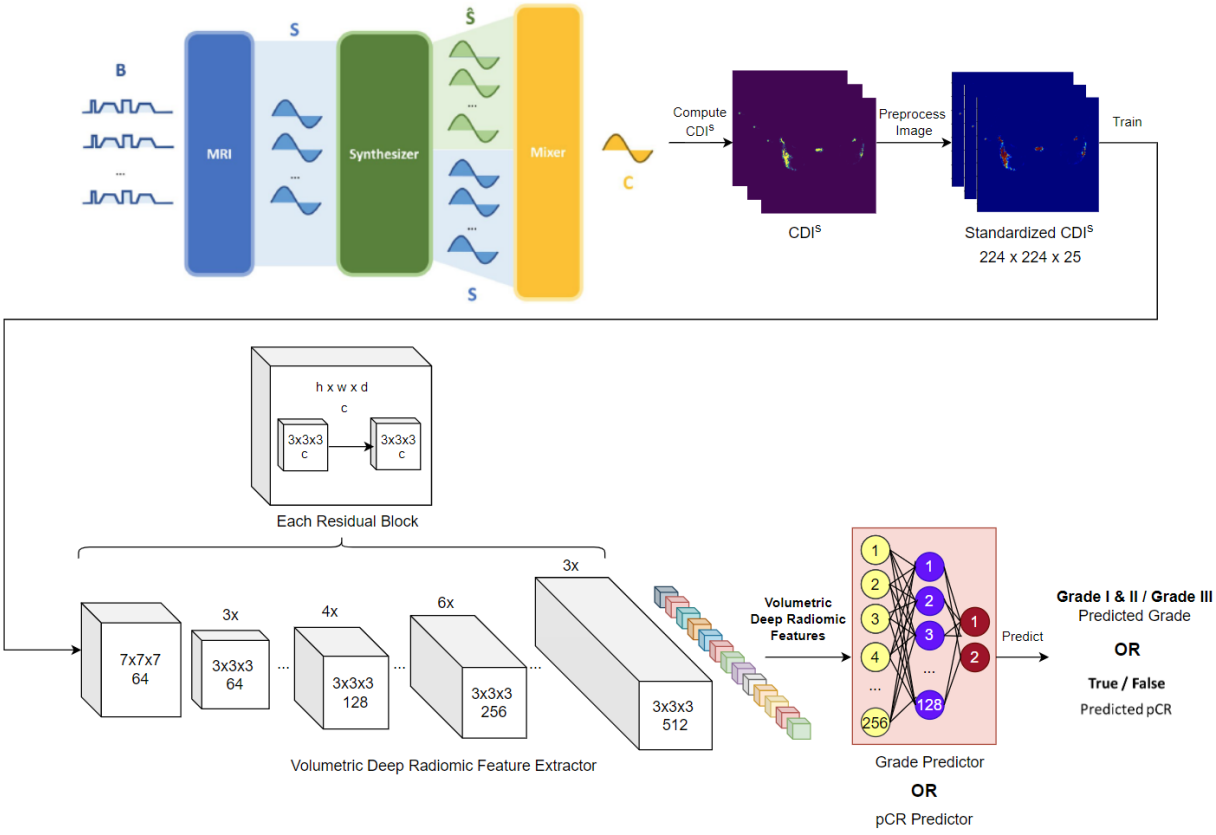

Figure 1.4: Proposed clinical support workflow for breast cancer using volumetric deep radiomic features from CDI^s.

Chapter 2

Background

This chapter provides a review of relevant background concepts, along with the patient data study. Section 2.1 describes the ACRIN 6698/I-SPY2 study. The data from the ACRIN 6698/I-SPY2 study is used in this thesis. Section 2.2 discusses the three different gold-standard MRI modalities studied in this thesis: diffusion-weighted imaging (DWI), apparent diffusion coefficient (ADC), and T2-weighted (T2w). Section 2.3 then presents synthetic correlated diffusion imaging (CDI^s) and how it has been applied to prostate cancer (PCa). Section 2.4 introduces the Residual Network (ResNet) model and Section 2.5 presents a description of Project Medical Open Network for AI (MONAI).

2.1 ACRIN 6698/I-SPY2 Study

The pre-treatment (T0) patient cohort in the ACRIN study was used as the patient cohort in this thesis [36, 37, 38, 39]. The timepoint T0 was selected as patients at this stage had not received any neoadjuvant chemotherapy and thus, the images would be most representative of the ones that pathologists would evaluate to determine SBR grade and decide if the patient should receive neoadjuvant chemotherapy.

The American College of Radiology Imaging Network (ACRIN) 6698/I-SPY2 study contains MRI images across 10 different institutions for patients at four different time-points in their treatment [36, 37, 38, 39]. The study provides the three main current gold-standard MRI modalities used in clinical practice: DWI acquisitions, T2w acquisitions, and ADC maps. The study also includes detailed annotation metadata (the lesion type, genetic subtype, longest diameter on the MRI (MRLD), the Scarff-Bloom-Richardson

(SBR) grade, and the post-treatment breast cancer pathologic complete response (pCR) to neoadjuvant chemotherapy). Manual DWI whole-tumor segmentations were identified using post-contrast DCE subtraction images and then localizing the regions on the ADC map [36, 37, 38, 39].

Patients in the ACRIN 6698/I-SPY2 study were imaged using either a 1.5 or 3.0 Tesla scanner with a dedicated breast radiofrequency coil and the scanner configuration was static for all images taken for a given patient. Imaging was done with the patient in the prone position and both the T2w sequence and DWI (b=0, 100, 600, 800 s/mm^2, 3-direction) were performed axially with full bilateral coverage. The pixel spacing for the acquisitions ranged from 0.83 mm to 2.08 mm with a median of 1.29 mm, with both slice thickness and spacing between slices ranged from 4.0 to 5.0 mm with a median of 4.0. ADC maps were then calculated based on the DWI data as a linear fit with ADC values below 0 or voxels below threshold set to 0 to suppress background pixels [36, 37, 38, 39].

Specific MRI acquisition parameters were used to obtain the T2w and DWI images for each patient in the ACRIN 6698/I-SPY2 study. Specifically, the reconstruction matrix was 512 by 512 for T2w and 256 by 256 for DWI with an in-plane resolution of less than or equal to 1.4 mm for T2w and from 1.7 to 2.8 mm for DWI. T2w was performed with active fat-sat recommended while DWI had a fat-suppression parameter value of active fat-sat. The flip angle for both T2w and DWI was 90 degrees with a slice thickness of less than or equal to 4 mm for T2w and between 4 to 5 mm for DWI. The number of slices for both MRI images was variable with complete bilateral coverage for T2w and bilateral coverage with adjustments to keep within a single acquisition for DWI. T2w also had a slice gap of less than or equal to 1.0 mm whereas there was no gap for DWI. The sequence acquisition time was less than or equal to 7 minutes for T2w images and between 4 to 6 minutes for DWI with no total post-contrast imaging duration. Four standardized b-values were used for DWI acquisitions at 0 s/mm^2, 100 s/mm^2, 600 s/mm^2, and 800 s/mm^2 [36, 37, 38, 39]. More details about the parameter values used to acquire T2w and DWI images are shown in Table 2.1 [36, 37, 38, 39].

The demographics of the dataset, filtered for patients with non-null pCR values, are shown in Table 2.2. It can be seen that the White race dominates the data, comprising of 70.8% of the patients in the dataset, illustrating a severe race bias towards White patients. Additionally, Figure 2.1 (top), it can be seen that the majority of the patients are between 30 to 70 years old (95.7%), indicating that very young patients (≤ 29) and very old patients (≥ 70) could be underrepresented in the dataset. On the other hand, the genetic subtype in the dataset is more fairly distributed with each subtype represented in at least 10% of the patients whereas the lesion type is more biased towards multiple masses and single mass as seen in Figure 2.2, upper left and right respectively. In addition, the longest diameter

Table 2.1: Table of MRI acquisition parameters used to obtain T2w and DWI images copied from [36, 37, 38, 39].

Parameter	T2-weighted	DWI
Sequence type	FSE or STIR	DW SE-EPI
2D or 3D sequence	2D	2D
Slice orientation	Axial or sagittal	Axial
Laterality	Bilateral	Bilateral
Frequency direction	A/P	A/P
Phase direction	R/L (axial) S/I (sagittal)	R/L
FOV – frequency	260-360 mm (axial) 180-220 mm (sagittal)	260-360 mm [a]
FOV - phase	300-360 mm (axial) 180-220 mm (sagittal)	300-360 mm [a]
Matrix – frequency (acquired)	256-512	128-192
Matrix – phase (acquired)	≥ 256	128-192
Reconstruction Matrix	512 x 512	256 x 256
In-plane resolution	≤ 1.4 mm	1.7 – 2.8 mm
Fat-suppression	Active fat-sat recommended	Active fat-sat
TR	2000-10000 ms	≥ 4,000 ms
TE	70-140 ms (STIR 70 ms)	Minimum (50-100ms)
Echo Train Length	≤ 16	N/A
TI (STIR sequence)	170 ms (1.5T) 230 ms (3.0T)	N/A
Flip Angle	90 degrees	90 degrees
Readout Bandwidth (per pixel)	N/A	N/A
b values	N/A	0, 100, 600, 800 s/mm^2
Slice thickness (acquired)	≤ 4 mm	4-5 mm
# of slices	Variable; complete bilateral coverage	Variable; bilateral coverage; adjust to keep w/in single acquisition
Slice Gap	≤ 1.0 mm	No gap
Parallel imaging factor	≤ 2	≥ 2
# of excitations/averages	≤ 2	≥ 2
k-space ordering	N/A	N/A
Sequence acquisition time	≤ 7 minutes	4-6 minutes (multi-b seq ~ 5 min)
Total post-contrast imaging duration	N/A	N/A

Table 2.2: Summary of race demographic in the dataset.

Race	**Percentage**
White	70.8%
Black	10.7%
Asian	6.3%
Unknown	11.1%
Multiple Races	0.4%
Native Hawaiian or other Pacific Islander	0.4%
American Indian or Alaska Native	0.4%

on the MRI (MRLD) is also biased towards the range of 2 to 4 cm with less representation from patients in the other diameter ranges as seen in Figure 2.1 (bottom).

The grade distribution and pCR division for patients filtered with non-null pCR values are shown in bottom half of Fig. 2.2, indicating an uneven distribution in SBR grade, significantly skewed towards Grade III (High) and shows that more patients with no pCR (67.6%) compared to those who achieved pCR after neoadjuvant chemotherapy (32.4%).

2.2 Current Gold-Standard MRI Modalities

Magnetic resonance imaging (MRI) is a non-invasive diagnostic imaging method that uses magnetic fields and radio waves to generate detailed images of body organs and tissues [40, 41]. For repeated imaging, MRI is considered a safer alternative to X-ray and computed tomography (CT) scans as it uses non-ionizing radiation as opposed to ionizing radiation [41, 42]. In this thesis, the performance with CDI^s is compared to that of three different gold-standard MRI modalities: diffusion-weighted imaging (DWI), apparent diffusion coefficient (ADC), and T2-weighted (T2w).

2.2.1 Diffusion-weighted Imaging (DWI)

Diffusion is the movement of water through tissue and is influenced by tissue density [10]. DWI is a form of MRI that measures the Brownian movement of water molecules within biological tissue using b values (0, 100, 600, 800), where each value signifies the strength of the diffusion sensitizing gradient [43]. A b value of 0 indicates no diffusion sensitivity,

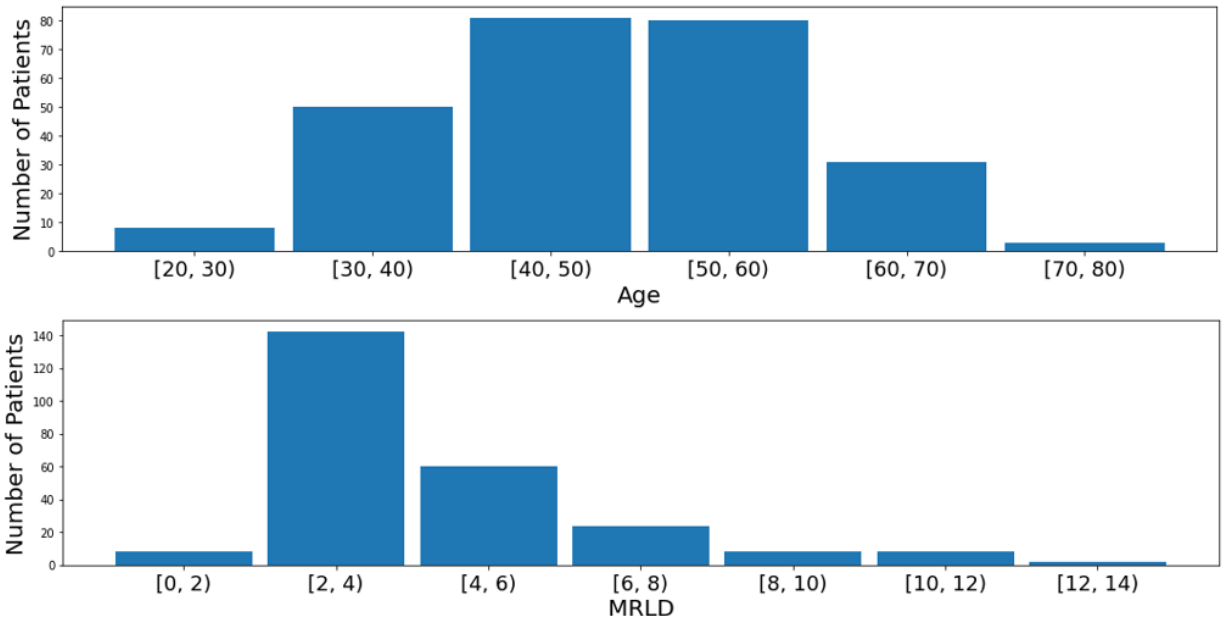

Figure 2.1: Distribution of the age (top) and longest diameter on the MRI (MRLD) in cm (bottom) for patients in the dataset.

and sensitivity increases with higher b values [10, 44, 45]. Introduced in the late 1980s, DWI has become pivotal in diagnosing and characterizing various medical conditions [46]. It plays a crucial role in the early identification of ischemic strokes, as well as in evaluating tumors and neurodegenerative diseases [47]. Figure 2.3 highlights the principle of DWI. In normal tissue (left panel of Figure 2.3), water is able to move freely which leads to a low DWI signal. On the other hand, in cancer tissue (right panel of Figure 2.3), the high cellularity restricts the movement of water which leads to a high DWI signal [48].

2.2.2 Apparent Diffusion Coefficient (ADC)

The quantitative measure derived from DWI is known as the apparent diffusion coefficient (ADC) [43]. ADC is obtained by taking the slope of the curve created with the different b values in DWI [43]. Hence ADC reflects the degree of water diffusion within the tissue, with lower ADC indicating regions with restricted diffusion or potentially cancerous tissue (as seen in Figure 2.3).

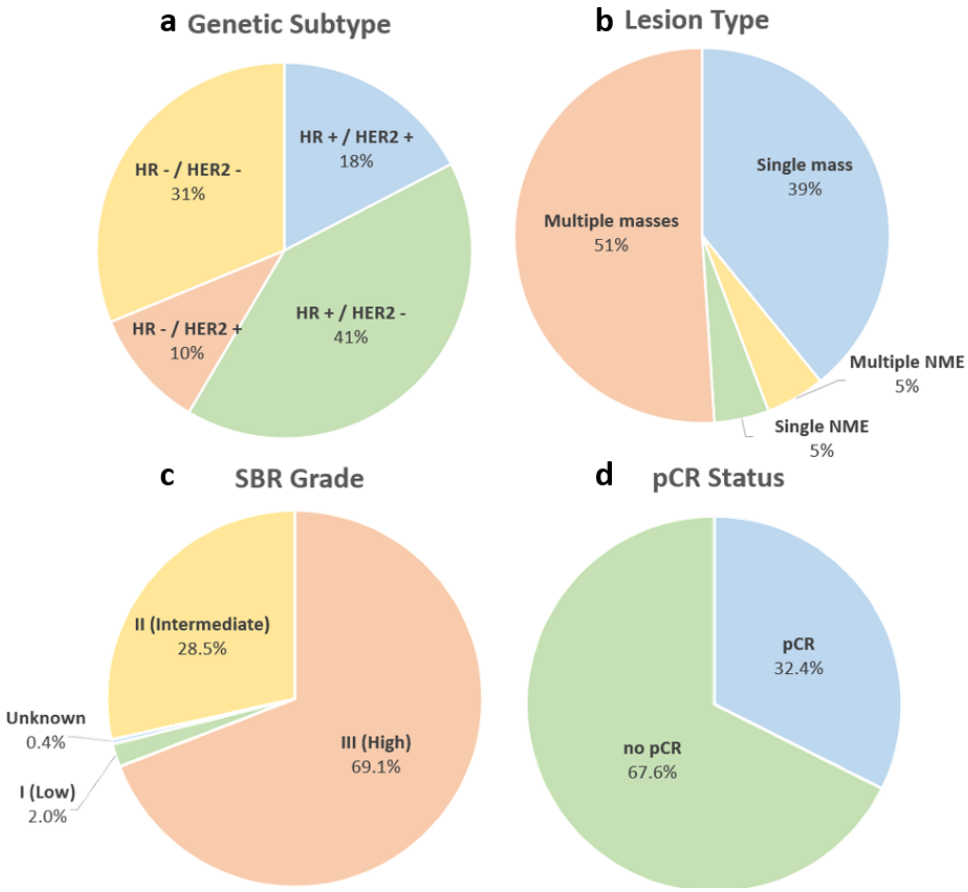

Figure 2.2: Patient distribution of genetic subtype (a), lesion type (b), SBR grade (c) and pCR status (d) in the dataset.

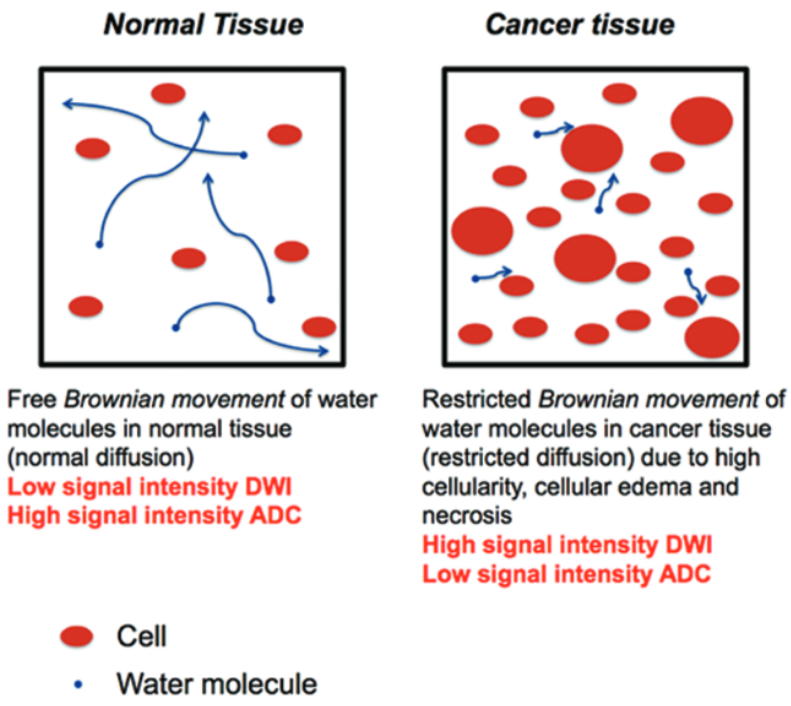

Figure 2.3: Conceptual illustration of the principle of DWI copied from [48].

Table 2.3: Table of the relationship between signal intensity and tissue type for T2w images copied from [52].

Signal intensity	Tissues
Dark	Air, mineral-rich tissue (cortical bone, stones), fast-flowing blood
Low	Collagenous tissue (ligaments, tendons, scars), bone islands
Low to intermediate	High bound water tissues (liver, pancreas, adrenals, hyaline cartilage, muscle)
Intermediate to bright	Fat, fatty bone marrow
Bright	High free water tissue (kidneys, gonads, edema, fluids [urine, bile], simple cysts, bladder, gallbladder, spleen, CSF). Proteinaceous tissue, blood products (oxyhemoglobin, extracellular methemoglobin)

2.2.3 T2-weighted (T2w)

T2-weighted (T2w) is a form of MRI that leverages transverse magnetization to distinguish between anatomical structures with different water content [49]. T2w focuses on the T2 relaxation time of tissues, which is the time it takes for protons in a tissue to lose their transverse magnetization [50]. Tissues affected by pathological processes typically exhibit higher water content than their normal counterparts [51]. Consequently, areas affected by conditions, accentuated by fluids like cerebrospinal fluid or vitreous humor, appear as bright regions on T2w images [52]. A tabular summary of the signal intensities for different tissues on T2w images is provided in Table 2.3.

2.3 Synthetic Correlated Diffusion-weighted Imaging

Correlated diffusion imaging (CDI) analyzes the direction of diffusion in the cancerous tissue [53] whereas synthetic correlated diffusion imaging (CDI^s) introduces synthetic signals by extrapolating MRI data to introduce more data points [10]. The methodology to compute CDI^s is shown in Figure 2.4 from [10]. The process begins with multiple native DWI signals obtained for different b values. These signals are then passed into a signal synthesizer which produces synthetic signals. The native signals are then mixed with the synthetic signals to obtain a final signal (CDI^s) [10].

When applied to prostate cancer (PCa) delineation, [10] showed promising preliminary results for CDI^s compared to current MRI techniques. In their extensive study [10], the

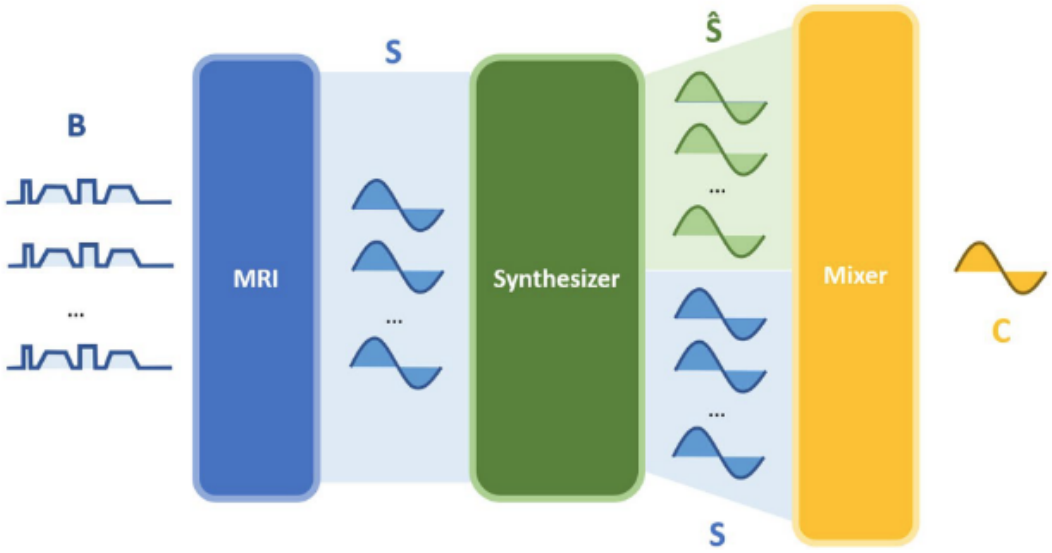

Figure 2.4: Process to compute CDI^s copied from [10].

authors explored the correlation between PCa presence and CDI^s. Using a cohort of 200 patient cases, the authors assessed the performance of CDI^s in delineating PCa against established MRI techniques (T2-weighted (T2w), diffusion-weighted imaging (DWI), and dynamic contrast-enhanced imaging (DCE)) [10]. Statistical analyses indicated that CDI^s hyperintensity served as a strong indicator of PCa presence, surpassing the delineation capabilities of T2w, DWI, and DCE [10].

2.4 Residual Network Model

A Residual Network (ResNet) is a deep learning architecture designed to address the challenge of training very deep neural networks [54]. ResNet uses the residual learning concept and introduces residual blocks, which contain shortcut connections that skip one or more layers. As a result, the model does not need to learn the direct mapping from input to output, but instead learns the residual mappings. As seen in Figure 2.5, the identity mapping is executed by the shortcut connections and the results are simply combined with the outputs of the stacked layers. Hence, the inclusion of identity shortcut connections does not bring about any additional parameters or significantly increase computational complexity. By having shortcut connections, the gradient can flow more easily through the

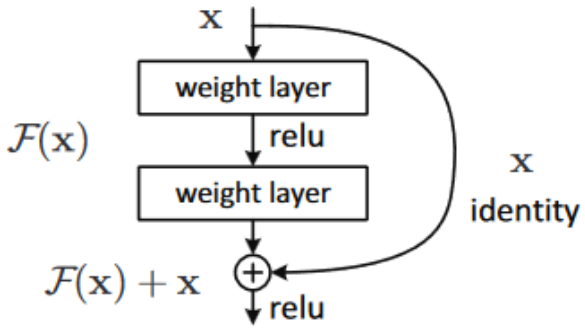

Figure 2.5: The building block in residual learning from [54].

network during backpropagation, making training and optimization more efficient and less complex compared to other networks like VGG net [54].

2.5 Project MONAI

Project Medical Open Network for AI (MONAI) is an open-source library containing PyTorch-based frameworks for employing deep learning in medical imaging [55]. Specifically, the library contains three different workflow tools: MONAI label (image labelling and learning), MONAI core (model training resources), and MONAI deploy (application packaging and deployment) [55]. In this thesis, the pretrained ResNet-34 model in MONAI core is used [56]. This pretrained model was trained on a large-scale 3D medical dataset 3DSeg-8, a consolidated dataset of images from eight publicly available 3D segmentation datasets containing both MRI and CT imaging modalities [56].

2.6 Summary

This chapter describes the relevant background about the patient data used throughout the thesis (from the ACRIN study) along with the three gold-standard MRI modalities: DWI, ADC, and T2w. This chapter also reviews CDI^s for better understanding of the computation and optimization of the CDI^s images in the next chapter. ResNet and MONAI are also introduced in this chapter as they are used in the proposed workflow for the clinical tasks of pCR prediction and SBR grade classification in subsequent chapters.

Chapter 3

Synthetic Correlated Diffusion Imaging (CDI^s) for Breast Cancer

In this chapter, the problem motivating the use of CDI^s is provided in Section 3.1. The methodology to compute CDI^s is provided in Section 3.2 and to create the multiparametric MRI is described in Section 3.3. Section 3.4 provides a brief summary of the chapter.

3.1 Problem Formulation

A new form of magnetic resonance imaging (MRI) called synthetic correlated diffusion (CDI^s) imaging was recently introduced and showed considered promise for clinical decision support for cancers such as prostate cancer when compared to current gold-standard MRI techniques such as T2-weighted (T2w) imaging, diffusion-weighted imaging (DWI), and dynamic contrast-enhanced (DCE) imaging [10]. However, the efficacy for CDI^s for other forms of cancer such as breast cancer has not been as well-explored nor have CDI^s data been previously made publicly available. Motivated to advance efforts in the development of computer-aided clinical decision support for breast cancer using CDI^s, this chapter investigates computing CDI^s for breast cancer.

3.2 Methodology

The pre-treatment cohort from the ACRIN study is used, with filtering for patients with non-null pCR values.

As described in [10], computing CDI^s involves the acquisition of multiple native DWI signals with different b-values. These native signals are then passed into a signal synthesizer to produce synthetic signals. The synthetic signal acquisitions relies on defining $\hat{S}$, the specific synthetic signals to acquire. Unlike [10], to create CDI^s for breast cancer, $\hat{S}$ was defined as [0, 1000, 2000, 3000, 4000, 5000] to account for the lower signal intensity for breast cancer images.

Finally, the native and synthetic signals produced via a signal synthesizer are mixed together to obtain a final CDI^s signal [10]. The calibrated signal mixing function uses ρ, which represents the coefficients that control the contribution of different gradient pulse strengths and timings to produce the CDI^s signal. The initial ρ values were defined as [1, 1, 1, 1, 1, 1], which were the base ρ values from [10].

Examples of the computed CDI^s is shown in Figure 3.1.

3.3 Multiparametric MRI Creation with CDIs

In literature, multiparametric MRIs have recently gained popularity as they have been shown to greatly benefit breast cancer clinical task enhancement with deep learning [57]. Multiparametric MRIs are created by fusing two or more MRI modalities together with the combination achieving better performance than each MRI modality on its own [58].

For this thesis, the CDI^s signals are fused with DWI to create a multiparametric MRI for each patient, represented by the term mpMRI^{cdis}. As seen in Figure 3.2, the multiparametric MRI leverages the structural information from DWI while keeping the important signals from CDI^s.

3.4 Summary

In this chapter, the process to compute CDI^s and mpMRI^{cdis} are described. Sample images for both the raw CDI^s and the mpMRI^{cdis} are also provided. The next chapter (Chapter 4) examines leveraging mpMRI^{cdis} for improving pCR for breast cancer.

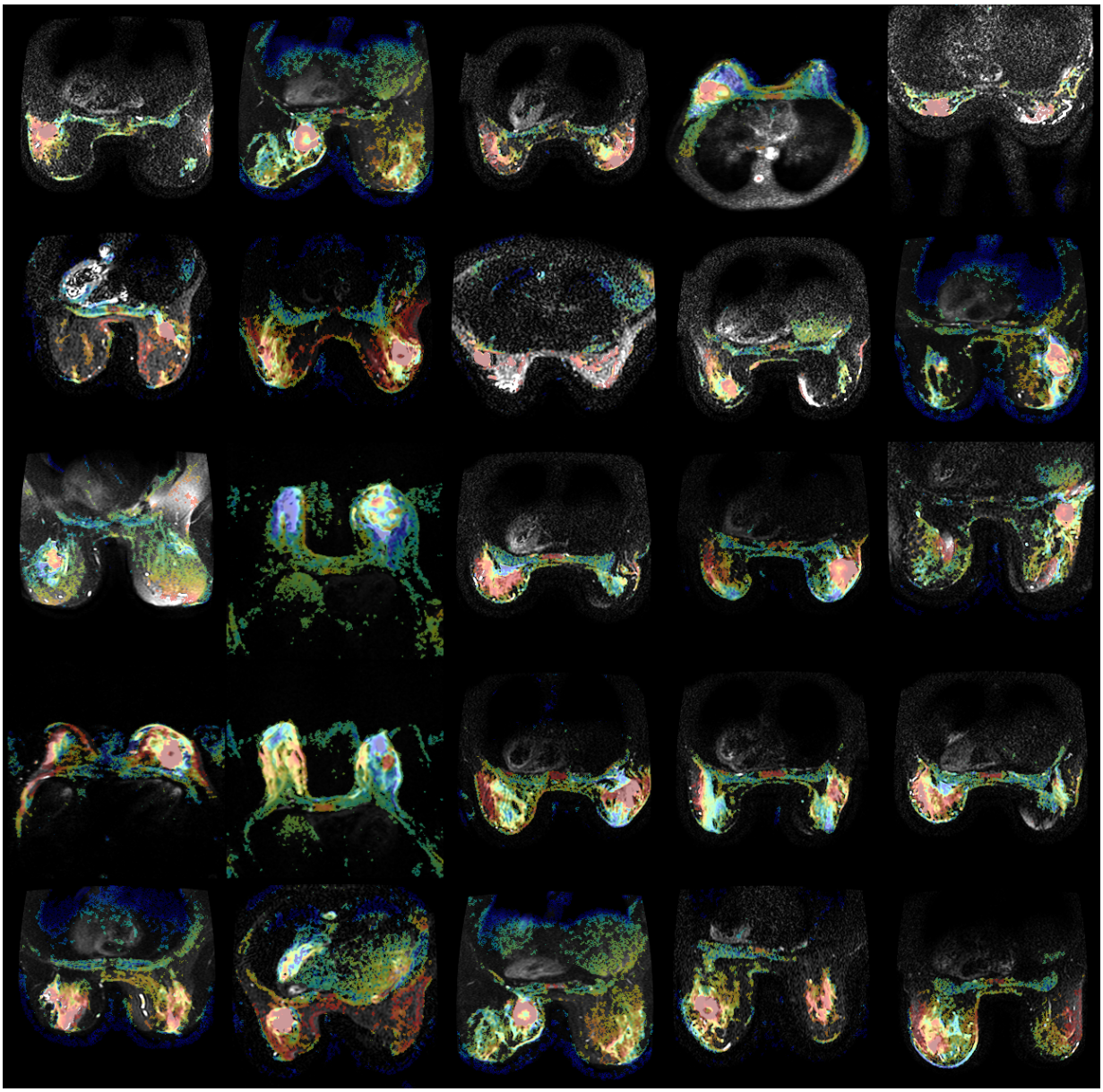

Figure 3.1: Example breast CDI^s.

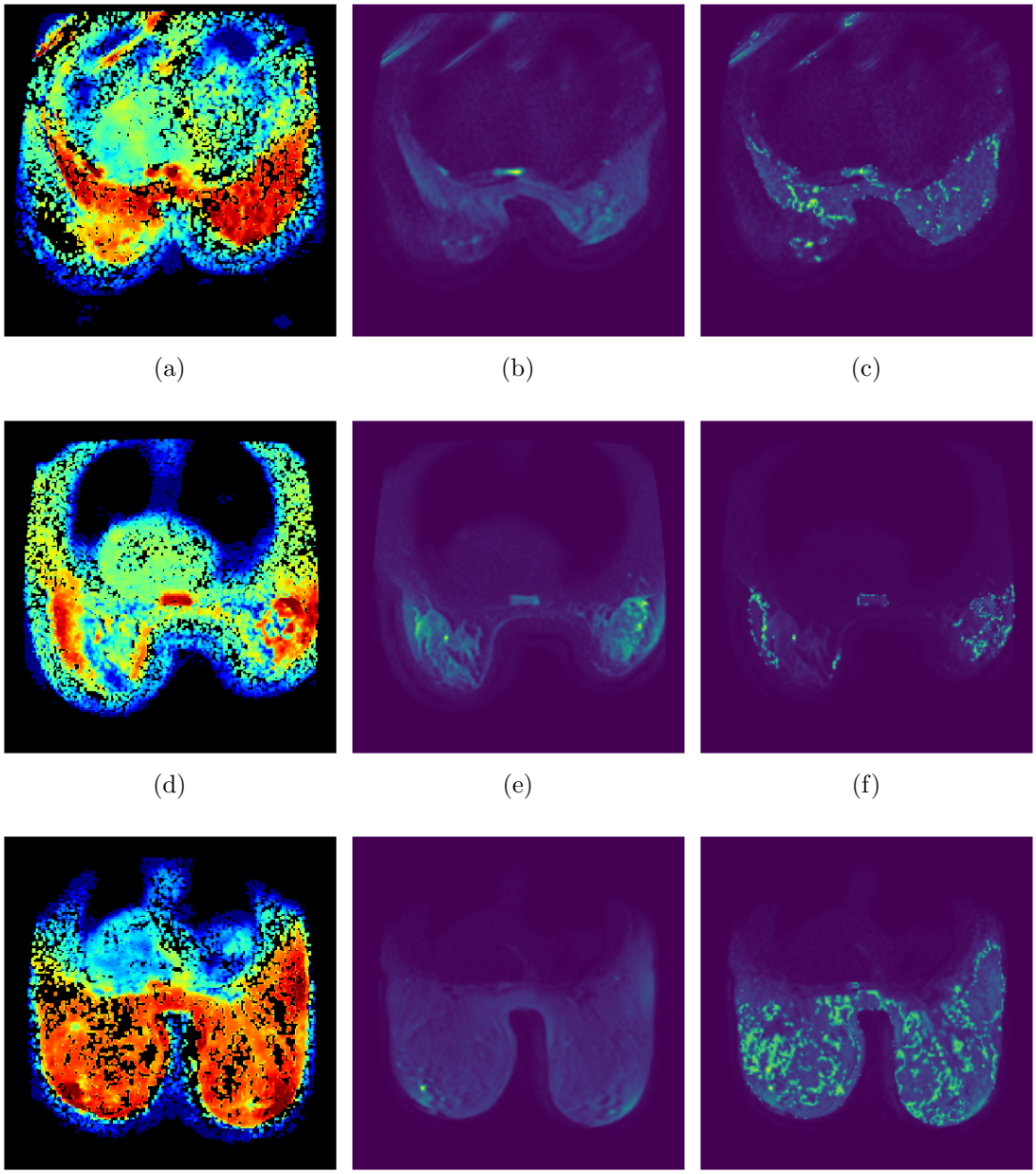

(a) (b) (c)

(d) (e) (f)

(g) (h) (i)

Figure 3.2: Sample CDI^{s} (a, d, i), DWI (b, e, h), and the combined mpMRI^{cdis} (c, f, i) for three different patients.

Chapter 4

Breast Cancer Pathologic Complete Response Prediction with CDI^s

This chapter discusses the proposed workflow for learning volumetric deep radiomic features from a pre-treatment cohort for pCR prediction with the problem formulation presented in Section 4.1. The experimental setup and results are described in Section 4.2 and Section 4.3, respectively. Section 4.4 provides a brief summary of the chapter.

4.1 Problem Formulation

Neoadjuvant chemotherapy has recently gained popularity as a promising treatment strategy for breast cancer, attributed to its efficacy in shrinking large tumors and leading to pathologic complete response. However, the current process to recommend neoadjuvant chemotherapy relies on the subjective evaluation of medical experts which contain inherent biases and significant uncertainty. Innovations in the field of cancer regarding computer vision and medical imaging have revealed promising methods for predicting pCR. Inspired by the positive outcomes of using CDI^s for prostate cancer delineation, this chapter investigates using CDI^s to enhance breast cancer pathologic complete response prediction.

4.2 Experimental Setup

Patients from the ACRIN study was used and patients with null pCR values were filtered from the dataset, with a total of 253 remaining patients. To compare the performance of

mpMRI^{cdis} with current gold-standard MRI modalities used in clinical practice, diffusion-weighted imaging (DWI) acquisitions, T2-weighted (T2w) acquisitions, and apparent diffusion coefficient (ADC) maps were also obtained from the ACRIN study. CDI^{s} acquisitions were computed for a given patient, as described in Chapter 3. These imaging acquisitions are then standardized into 224×224×25 volumetric data cubes to achieve dimensionality consistency for machine learning purposes.

Next, motivated by the advances in deep learning as well as the volumetric nature of CDI^{s} data, a 34-layer volumetric residual convolutional neural network architecture was constructed and leveraged to learn volumetric deep radiomic features from the standardized volumetric data cubes [59]. The aim with leveraging volumetric deep learning at this stage is to, rather than design hand-crafted radiomic features, directly learn volumetric deep radiomic features from patient data that characterizes the intrinsic properties of breast cancer tissue as captured by CDI^{s} that are relevant as it relates to patient pCR to neoadjuvant chemotherapy after pre-treatment imaging. This volumetric neural network can then be used to produce deep radiomic features for each patient based on their patient image data cubes. Finally, a pCR predictor comprising of a fully-connected neural network architecture is then learnt based on the extracted deep radiomic feature and patient post-treatment pCR data, and subsequently used to predict patient pCR post-treatment to neoadjuvant chemotherapy.

To evaluate the efficacy of the proposed approach, we conducted leave-one-out cross-validation (LOOCV) on the patient cohort with accuracy being the performance metric of interest. For comparison consistency, a separate volumetric deep radiomic feature extractor and pCR predictor (with the same network architectures as for mpMRI^{cdis} as described in the Method section) was used to learn a set of volumetric deep radiomic features from each gold-standard MRI modality (DWI, T2w, and ADC). Notably, we also leveraged DWI acquisitions in two different ways: 1) individual sets of features are learnt from DWI acquisitions of each b-value (b=0, 100, 600, 800), and 2) an individual set of features are also learnt from the combined stack of DWI acquisitions (namely, the b-values are treated as another channel in the input).

4.3 Experimental Results

As seen in Table 4.1, with the exception of ADC, leveraging volumetric deep radiomic features from each of the imaging modalities achieved pCR predictive accuracy over 80% with the highest accuracy obtained from the multiparametric MRI with CDI^{s}, mpMRI^{cdis}. With an improvement in accuracy of over 3% compared to the next highest modality

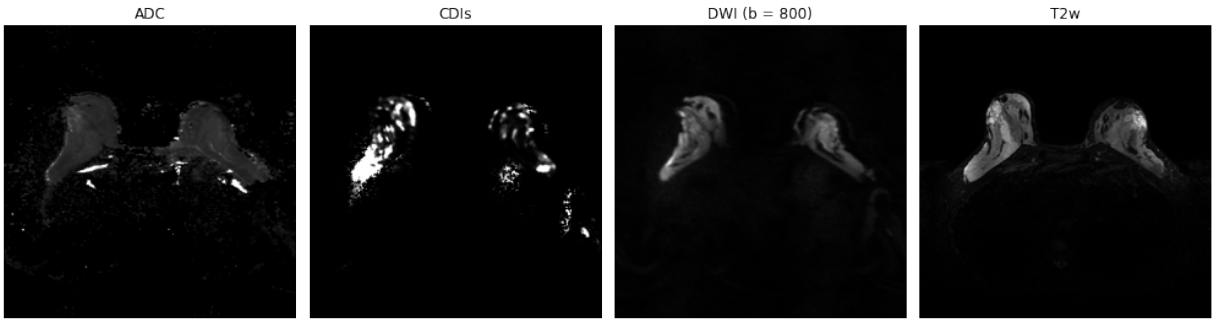

Figure 4.1: Example slice illustrating visual differences between ADC, mpMRI^{cdis}, DWI, and T2w before neoadjuvant chemotherapy for a patient who experienced pCR. In this patient case, pCR prediction was correct for CDI^{s} and DWI b = 800 but not the other modalities.

Table 4.1: pCR prediction accuracy using LOOCV for different imaging modalities.

Imaging Modality	Accuracy (%)
mpMRI^{cdis}	**87.75**
ADC	79.84
T2w	83.79
DWI (b=0, 100, 600, 800)	84.19
DWI (b=0)	84.19
DWI (b=100)	82.21
DWI (b=600)	84.19
DWI (b=800)	84.58

(i.e., DWI b = 800), mpMRI^{cdis} outperforms the gold-standard imaging modalities. An illustrative example highlighting the visual differences between the imaging modalities of ADC, mpMRI^{cdis}, DWI b = 800, and T2w for a patient case where pCR prediction was correct for mpMRI^{cdis} and DWI (b=800) but not the other modalities is shown Figure 4.1.

4.4 Summary

In this chapter, the efficacy of leveraging volumetric deep radiomic features to predict pCR for breast cancer patients considering neoadjuvant chemotherapy was investigated. Evaluation using a pre-treatment cohort showed that the proposed approach can increase

the pCR prediction performance compared to gold-standard MRI modalities. Specifically, the volumetric deep radiomic features learnt with mpMRI$^{\text{cdis}}$ enabled a pCR prediction accuracy of 87.75%, which is over 3% above the next best gold-standard MRI modality. Given the promising results, the next chapter examines leveraging mpMRI$^{\text{cdis}}$ for SBR grade classification.

Chapter 5

Breast Cancer Scarff-Bloom-Richardson Grade Classification with CDI^{s}

This chapter reviews using the proposed workflow for learning volumetric deep radiomic features from a pre-treatment cohort for SBR grade prediction. Section 5.1 formulates the problem for SBR grade prediction. Section 5.2 sets up the experimental design and Section 5.3 presents the experimental results. Finally, Section 5.4 summarizes the chapter.

5.1 Problem Formulation

Grading is a crucial factor in breast cancer treatment planning, but the current method to grade breast cancer tumors involves tissue extraction from the patient which causes patient stress and discomfort [60], along with high medical fees [61]. In addition, the current method to determine the cancer grade is based on a human pathologist's opinion [12]. With potential biases and high uncertainty in clinical judgement, it is possible for the patient to receive an incorrect grade leading to an unsuitable treatment strategy [27]. Recent advancements in computer vision and imaging in the cancer domain have shown promise of noninvasive ways to diagnose and evaluate cancer tumours with high accuracy. Hence, a need exists to noninvasively identify breast cancer grades in an accurate and quick manner.

5.2 Experimental Setup

The T0 patient cohort in the ACRIN study was used as the patient cohort in this study [36, 37, 38, 39]. 252 patient cases remained when patients who had any incomplete data were removed. As seen in Table 5.1, there is an uneven distribution of patients between the three grades and hence, SBR grade I and II were combined into one category.

Table 5.1: SBR grade distribution in the patient cohort.

SBR Grade	**Number of Patients**
Grade I (Low)	5
Grade II (Intermediate)	72
Grade III (High)	175

DWI, ADC, and T2w were obtained directly from the ACRIN study for the patients. The multiparametric MRI is created using the CDI^s computed from the DWI images as described in Chapter 3. For SBR grade classification, the ResNet model is initialized with the model weights from Chapter 4, which were obtained by training for pCR prediction. To achieve dimensional consistency for machine learning, the images are standardized into 224x224x25 volumetric data cubes for each patient.

Notably, the ResNet model is a 34-layer volumetric residual convolutional neural network architecture leveraged to learn volumetric deep radiomic features from the standardized volumetric data cubes. The aim with leveraging volumetric deep learning at this stage is to, rather than design hand-crafted radiomic features, directly learn volumetric deep radiomic features from patient data that characterizes the intrinsic properties of breast cancer tissue that are relevant as it relates to SBR grading. This volumetric neural network can then be used to produce deep radiomic features for each patient based on their data cubes. Finally, a grading classifier comprising of a fully-connected neural network architecture is then learnt based on the extracted deep radiomic feature and SBR grading data, and subsequently used to predict the patient SBR grade. For comparison consistency, a separate volumetric deep radiomic feature extractor and grade predictor (with the same network architectures) was used to learn a set of volumetric deep radiomic features from each modality.

To evaluate the efficacy of the proposed approach, leave-one-out cross-validation (LOOCV) was conducted on the patient cohort with accuracy being the performance metric of interest. Other measured quantitative metrics include sensitivity, and specificity. Sample

illustrative examples highlighting the visual differences between the imaging modalities for patients where the grade prediction was correct for the mpMRI^{cdis} but not the other gold-standard modalities are also included.

5.3 Experimental Results

As seen in Table 5.2, leveraging volumetric deep radiomic features for mpMRI^{cdis} achieves the highest grade predictive accuracy of 87.7% with both sensitivity and specificity values over 80%. Furthermore, mpMRI^{cdis} outperforms the gold-standard imaging modalities with an improvement of over 10% on the next highest modality (T2w). With the highest gold-standard MRI modality only achieving a prediction accuracy of 76.59%, over 10% lower than mpMRI^{cdis}, the proposed approach with mpMRI^{cdis} can increase the grade prediction performance compared to gold-standard MRI modalities. Notably, mpMRI^{cdis} exhibits lower sensitivity compared to other modalities, indicating that it has a lower ability to accurately classify patients as SBR grade III. On the other hand, while the other modalities demonstrate higher sensitivity, they suffer from significantly lower specificity, leading to inaccurate identification of patients as SBR grade I/II. For this clinical task, both sensitivity and specificity are paramount to ensure appropriate treatment allocation. This ensures that patients with more aggressive cancer tumors receive necessary treatment while minimizing unnecessary treatments and potential side effects for those with less severe tumors [62]. Hence, mpMRI^{cdis} has a better overall performance compared to the other modalities. An illustrative example highlighting the visual differences between the imaging modalities of ADC, mpMRI^{cdis}, DWI b = 800, and T2w for a patient case where grade prediction was correct for mpMRI^{cdis} but not the other modalities is shown Figure 5.1.

Table 5.2: SBR grade prediction accuracy using LOOCV for different imaging modalities.

Modality	**Accuracy**	**Sensitivity**	**Specificity**
mpMRI^{cdis}	**87.70%**	**90.29%**	**81.82%**
T2w	76.59%	99.43%	24.68%
ADC	69.44%	100.00%	0.00%
DWI	69.44%	95.43%	10.39%

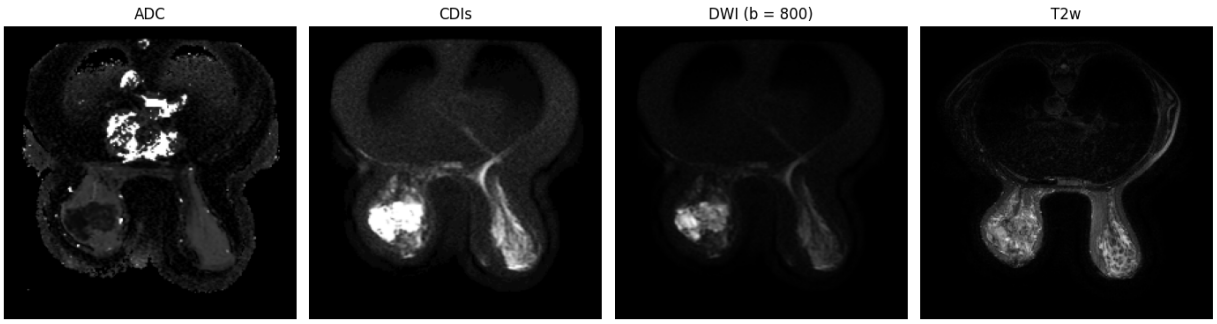

Figure 5.1: An example slice illustrating visual differences between ADC, mpMRI^{cdis}, DWI, and T2w at pre-treatment for a patient who has SBR Grade II (Intermediate). In this patient case, grade prediction was correct for mpMRI^{cdis} but not the other modalities.

5.4 Summary

In this chapter, the volumetric deep radiomics approach for predicting SBR grade based on volumetric mpMRI^{cdis} data was compared to that based on other gold-standard MRI modalities. The multiparametric MRI with CDI^{s} achieved a categorized grade prediction accuracy of 87.70%. With the highest gold-standard MRI modality only achieving a prediction accuracy of 76.59%, over 10% lower than mpMRI^{cdis}, the proposed approach with mpMRI^{cdis} can increase the grade prediction performance compared to gold-standard MRI modalities. Given the promising results, the next few chapters focuses on CDI^{s} coefficient optimization and using optimized CDI^{s} to enhance clinical support for breast cancer.

Chapter 6

CDI^s Optimization for Breast Cancer Tumour Delineation

This chapter provides the description of the computation and optimization of CDI^s images for the patients. Specifically, the problem formulation, experimental setup, and experimental results are described in Section 6.1, Section 6.2, and Section 6.3, respectively. Section 6.4 provides a brief summary of the chapter.

6.1 Problem Formulation

Though CDI^s served as a strong indicator for PCa presence in tissue [10], there exists a few challenges for implementing CDI^s for BCa.

As defined in [10], there are two key components for computing CDI^s: (1) the calibrated signal mixing function and (2) synthetic signal acquisitions which are mixed with native signal acquisitions. The first component uses ρ, which are coefficients that control the contribution of different gradient pulse strengths and timings to produce the CDI^s signal. The second component relies on defining $\hat{S}$, the specific synthetic signals to acquire.

However, the challenge of what values to use for ρ and $\hat{S}$ are non-trivial as these values largely impact the quality of the CDI^s signal. Selecting optimal parameters by hand is not only labor-intensive but also time-intensive, making it advantageous to identify a strategy for optimizing these parameters for the specific task. Notably, it is also important that ρ does not have values that are too large as the mixing function used in computing CDI^s

combines signals multiplicatively and overflow errors would occur if the ρ values are too high.

In [10], the authors used $\rho = 1$ as their baseline form and also attempted to tune the coefficients ρ by maximizing the area under the receiver operating characteristic curve (AUC) using a Nelder-Mead simplex optimization strategy. For their synthetic signal acquisitions, they chose $\{1000 \text{ s/mm}^2, ..., 7000 \text{ s/mm}^2\}$ (at $1000 s/mm^2$ intervals) with a native signal acquisition at $b = 50 s/mm^2$. In the context of BCa, the initial native signal capture occurs at $b = 0 s/mm^2$, and these signals are not as intense as those in PCa.

Another challenge arises for optimizing these parameters; optimization of these parameters with AUC relies distinguishing between healthy and cancerous tissue. Unlike [10], the dataset used in this thesis only has the tumour mask and does not have the respective organ mask (mask of the breast) in the MRI images.

6.2 Experimental Setup

In terms of optimization setups, two main configurations were examined based on [10] and the specific task of BCa. Bounds of [-10, 10] were also added for ρ in the optimization to avoid overflow errors when computing CDI^s.

1. PCa Structure:
    - initial $\rho = [1.6160, 1.5209, 1.2006, 0.8362, 1.1630, 0.8666, 1.1424, -0.4635]$, the optimized ρ values from [10] (showing rounded values for brevity)
    - $\hat{S} = [50, 1000, 2000, 3000, 4000, 5000, 6000, 7000]$
2. BCa Structure (adjusted form of based on signal intensity and BCa use case):
    - initial $\rho = [1, 1, 1, 1, 1, 1]$, the base ρ values from [10]
    - $\hat{S} = [0, 1000, 2000, 3000, 4000, 5000]$

Optimization for both the two main configurations were conducted on the the processed MRI images. The processed images are standardized forms of the raw images that reduce each MRI volume to 25 slices, the minimum number of slices across all patients, and resize each image to 224 x 224.

The results from these two setups were compared to the unoptimized form that uses the base $\rho = [1, 1, 1, 1, 1, 1]$ values and $\hat{S} = [0, 1000, 2000, 3000, 4000, 5000]$.

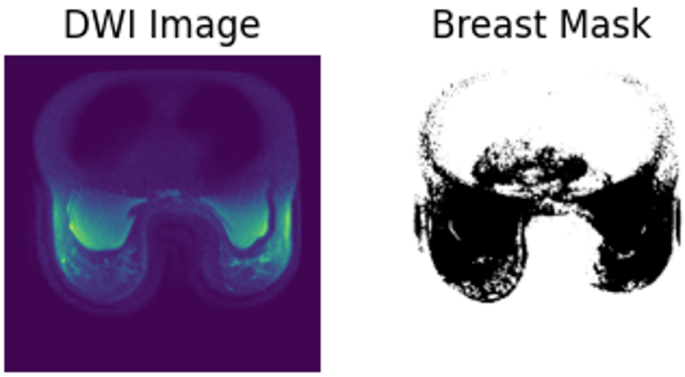

Figure 6.1: Sample breast mask generated from the DWI image.

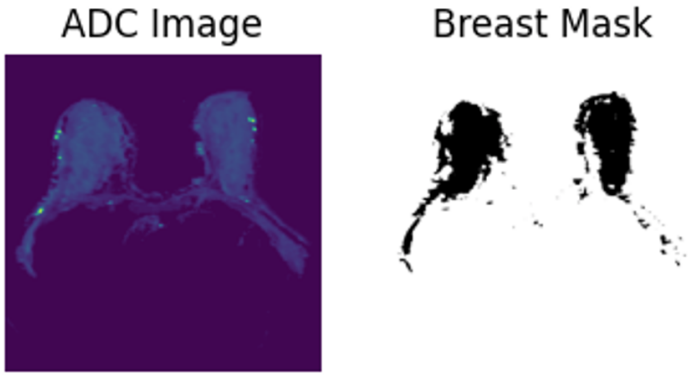

Figure 6.2: Sample breast mask generated from the ADC image.

To compute the breast mask, thresholding on the images were leveraged along with manual inspection of the resulting breast segmentation mask for quality. Since the signals for ADC and DWI are different, thresholding on both types of images were calculated to generate two types of breast masks. Notably the MRI modality T2w was not considered as there was no tumour mask for T2w images, which are configured significantly differently from DWI images. Example of breast images created from ADC and DWI are shown in Figure 6.2 and 6.1 respectively.

Similar to [10], the Nelder-Mead simplex optimization strategy was used to maximize the area under the receiver operating characteristic curve (AUC) for ability to delineate between healthy and cancerous breast tissue [63]. Though the Nelder-Mead simplex optimization strategy is not guaranteed to find the global minimum and may falsely converge

Table 6.1: PCa structure optimized parameters.

Configurations	**Optimized ρ Values**							
$\hat{S}$	**50**	**1000**	**2000**	**3000**	**4000**	**5000**	**6000**	**7000**
Initial Values	1.6160	1.5209	1.2006	0.8362	1.1630	0.8666	1.1424	-0.4635
ADC	4.1718	10.0000	0.4269	2.1377	1.8285	-1.3247	-4.3591	3.5843
DWI	3.5165	3.1218	1.7395	0.9957	0.6072	0.8040	-1.1245	-0.6547

Table 6.2: BCa structure optimized parameters.

Configurations	**Optimized ρ Values**					
$\hat{S}$	**0**	**1000**	**2000**	**3000**	**4000**	**5000**
Initial Values	1.0000	1.0000	1.0000	1.0000	1.0000	1.0000
ADC	9.8405	9.9514	-0.8604	-1.2513	4.7429	-0.0038
DWI	9.4760	0.0165	-0.7469	8.0292	0.8005	-4.9182

at another point, it is computationally compact and highly opportunistic, leading to its widespread popularity and use [63].

Both quantitative and qualitative evaluation is conducted. Quantitatively, the AUC values using the gold-standard MRI modalities of ADC and DWI b = 800 are compared against that of CDI^s. Qualitatively, histogram analysis is provided of ADC, DWI b = 800, and CDI^s values for healthy tissue and cancerous tissue. Lastly, some sample patient images for the various modalities are also shown to highlight their visual differences.

6.3 Experimental Results

6.3.1 Exponent Values

The optimized ρ values for the various optimization structures are provided below in Table 6.1 and 6.2 for the PCa and BCa (adjusted form from PCa based on signal intensity) structure, respectively. As seen, there is a significant difference in the optimized ρ values based on the type of breast mask used and whether optimization was conducted on the raw images themselves or the processed images. The optimized ρ values are also very different between the PCa and BCa optimization structure, even for the same $\hat{S}$ value.

Table 6.3: AUC values for the various modalities to separate healthy and tumour tissue with the best result bolded.

Modality	**AUC**
ADC	0.8323
DWI	0.9426
Unoptimized CDI^s	0.9224
Optimized PCa (ADC) CDI^s	0.9469
Optimized PCa (DWI) CDI^s	**0.9470**
Optimized BCa (ADC) CDI^s	0.9455
Optimized BCa (DWI) CDI^s	0.9437

6.3.2 AUC Values

Table 6.3 shows the AUC values for the various modalities to separate healthy and tumour tissue. Interestingly, the best AUC value on the processed images is achieved by the optimized PCa - DWI CDI^s modality. On the other hand, the second highest AUC value for processed AUC is obtained by optimized PCa - ADC CDI^s. Notably, the DWI modality achieves a 0.0044 decrease from the best processed AUC value.

6.3.3 Histogram Results

To study the distribution of ADC, DWI, CDI^s, and the optimized forms for CDI^s for healthy tissue and tumour tissue, histogram analysis was conducted. Figure 6.3 and 6.4 shows the histogram analysis for the MRI modalities (ADC, DWI, and unoptimized CDI^s) values for healthy tissue and tumour tissue using the ADC breast mask and DWI breast mask, respectively. Figure 6.5, and 6.6 shows the histogram analysis for the PCa and BCa optimized values for CDI^s values for healthy tissue and tumour tissue. These histograms use the respective breast mask that was used for optimization, e.g., PCa optimized CDI^s based on processed DWI is analyzed using the DWI breast mask.

6.3.4 Visual Comparison

This subsection shows the visual comparison of the various modalities studied in this section. Figure 6.7 shows the visual comparison of the tumour mask and the MRI modalities

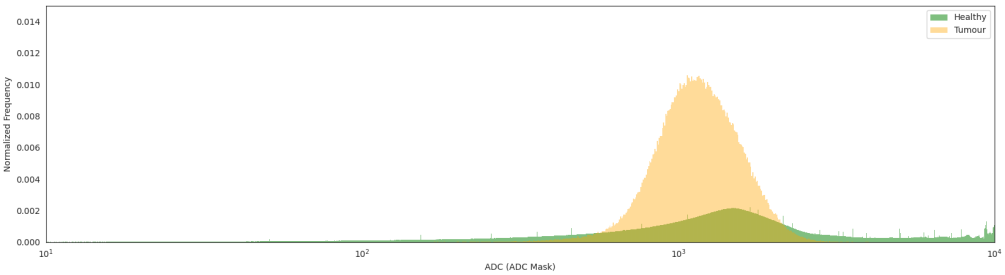

(a)

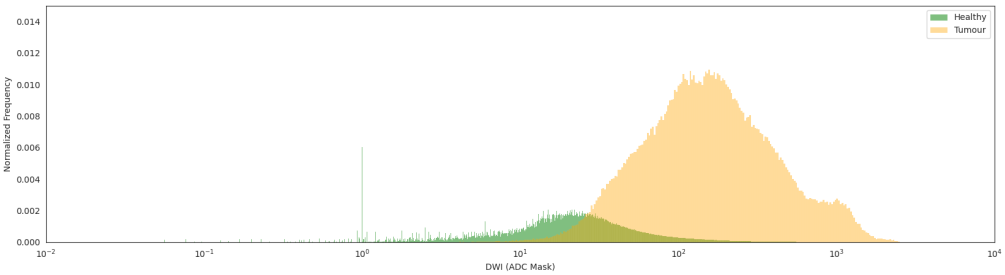

(b)

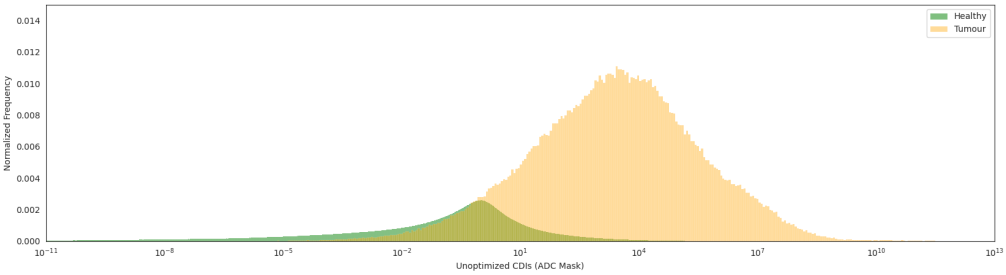

(c)

Figure 6.3: Histogram analysis for the MRI modalities (ADC, DWI, and unoptimized CDI^s) values for healthy tissue (green) and tumour tissue (orange) using the ADC breast mask.

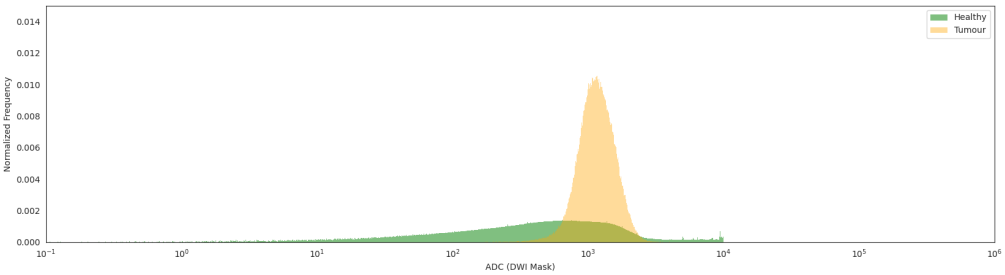

(a)

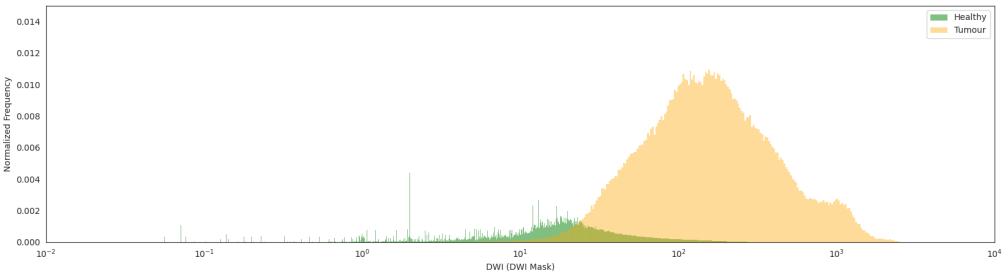

(b)

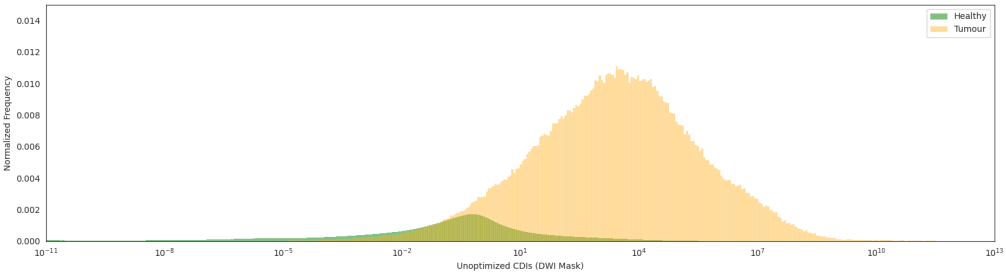

(c)

Figure 6.4: Histogram analysis for the MRI modalities (ADC, DWI, and unoptimized CDI^{s}) values for healthy tissue (green) and tumour tissue (orange) using the DWI breast mask.

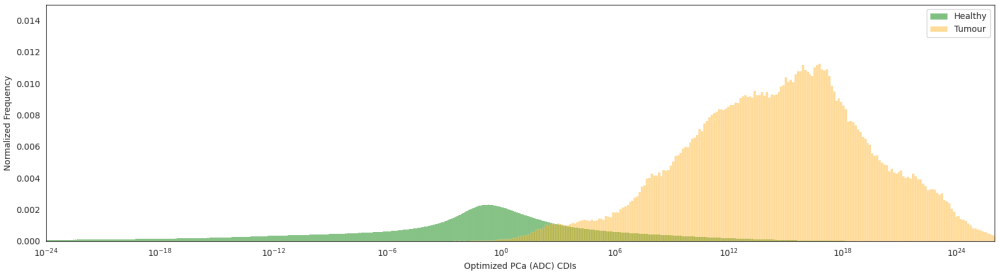

(a)

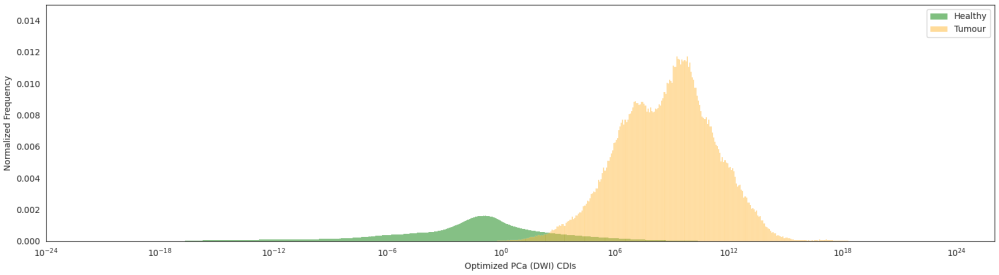

(b)

Figure 6.5: Histogram analysis for the PCa optimized values for CDI^s values for healthy tissue (green) and tumour tissue (orange) plotted with a log scale.

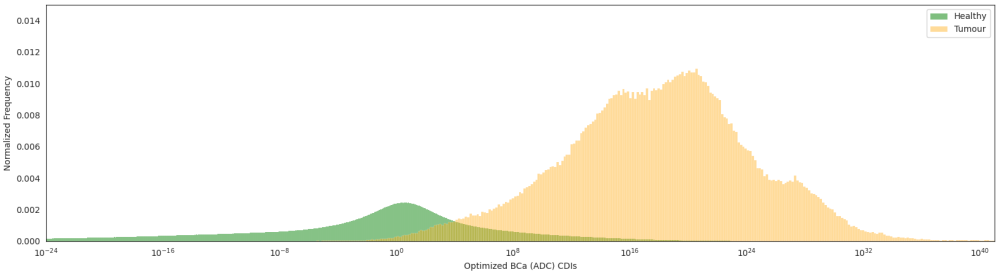

(a)

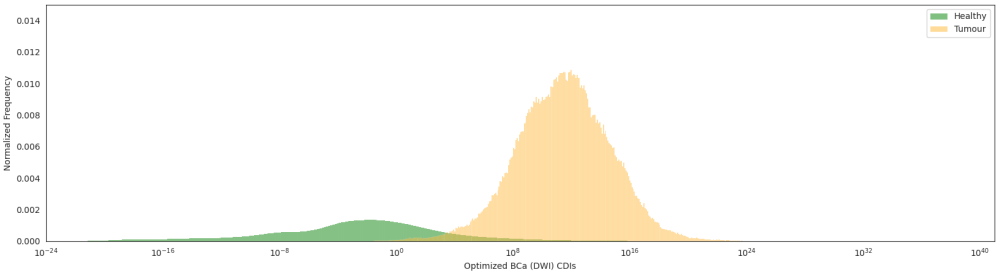

(b)

Figure 6.6: Histogram analysis for the BCa optimized values for CDI^s values for healthy tissue (green) and tumour tissue (orange) plotted with a log scale.

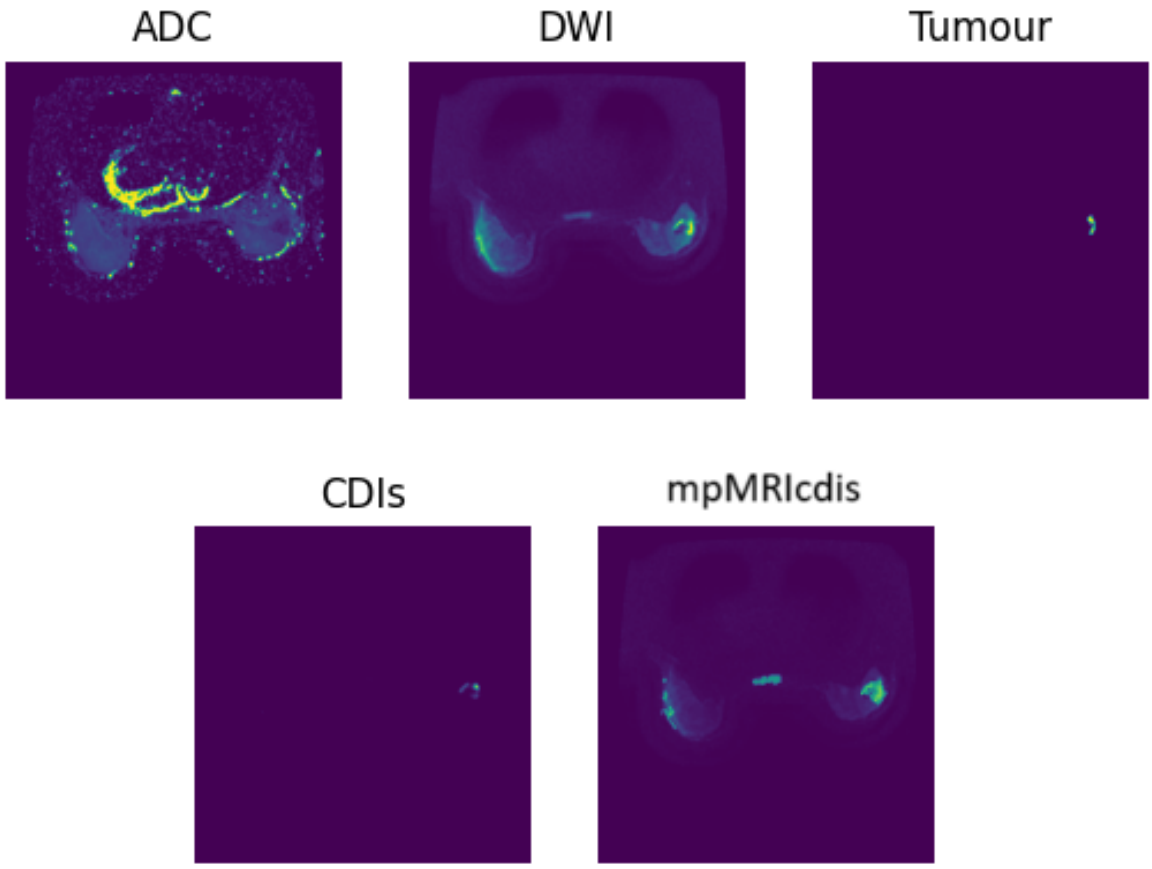

Figure 6.7: Visual comparison of the tumour mask, the MRI modalities (ADC, DWI, and unoptimized CDI^s), and mpMRI^{cdis}.

(ADC, DWI, and unoptimized CDI^s). As seen in Figure 6.7, CDI^s is able to capture the tumour region with the least amount of noise compared to the other modalities but does not contain any structural information about the corresponding breast.

Figure 6.8, and 6.9 show the visual comparison for the different optimized PCa and BCa parameters for CDI^s respectively. Notably, the CDI^s images do not contain any breast structural information, but shows the impact of selecting different ρ values as some CDI^s images have more noise compared to others and some are better able to highlight the tumour region.

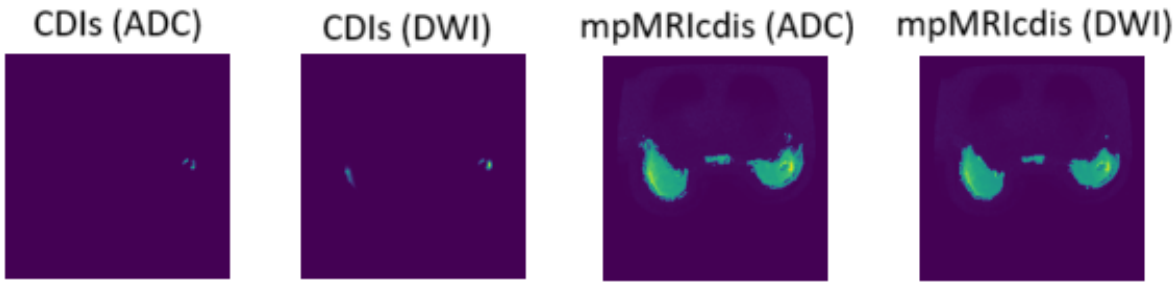

Figure 6.8: Visual comparison of the different optimized PCa parameters for CDI^s and the associated $mpMRI^{cdis}$.

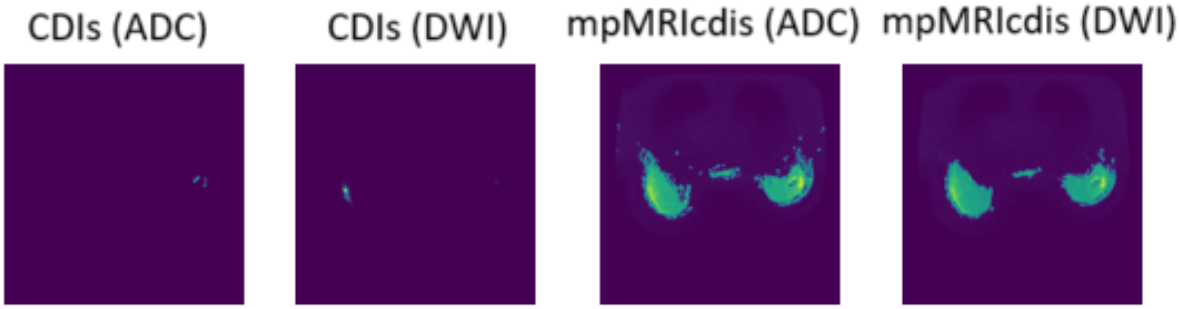

Figure 6.9: Visual comparison of the different optimized BCa parameters for CDI^s and the associated $mpMRI^{cdis}$.

6.4 Summary

CDI^s has recently been introduced as a strong indicator for PCa presence in tissue, motivating its application to other cancer domains like BCa. However, computing CDI^s requires two main components: ρ and $\hat{S}$ values to capture the contribution coefficients and specific synthetic signals to acquire, respectively.

Optimization for ρ values using two different sets of $\hat{S}$ values (one for the original PCa setup, and one adapted for BCa) showed that the CDI^s signal achieved a 0.0044 increase in AUC for processed images over the best gold-standard MRI modality (DWI). Notably, the optimized CDI^s modality achieves AUC values over 0.02 higher than the unoptimized CDI^s value, demonstrating the importance of optimizing the CDI^s exponents for the specific cancer application.

In addition to separating healthy and tumour tissue for breast, another important clinical BCa task is SBR grade classification. Although promising results were achieved using CDI^s for tissue separation, speculation arises about whether using optimized CDI^s would also provide enhancement for clinical support for breast cancer. This question is explored in the next chapter, Chapter 7.

Chapter 7

Clinical Support Enhancement for Breast Cancer with Optimized CDI^s

7.1 Problem Formulation

In previous chapters, leveraging volumetric deep radiomic features from synthetic correlated diffusion imaging (CDI^s) fused with DWI for breast cancer grade prediction showed promise compared to other MRI modalities, achieving a pCR prediction accuracy of 87.70% (Chapter 4) and a SBR grade classification accuracy of 87.75% (Chapter 5).

However, modifications to CDI^s for breast cancer were minimal, lacking proper tuning of the coefficients. Inspired by the positive outcomes of optimizing CDI^s for prostate cancer delineation [10] and the positive improvements from the previous chapter (Chapter 6) for breast cancer tumour delineation, this chapter investigates the application of optimized CDI^s to enhance the two studied clinical support tasks (pCR prediction and SBR grade classification).

7.2 Pathologic Complete Response Prediction

The data used is from the ACRIN study filtered for non-null pCR values, with a total of 253 patients remaining. As the classes were imbalanced (class 0:1 is 67.6%:32.4%), a weighted random sampler was added to the training sampler along with an AdamW optimizer. In addition, a cosine annealing learning rate scheduler was also implemented during training.

The optimized CDI^s signals from Chapter 6 were fused with DWI to create a multiparametric MRI, mpMRI^{cdis}. Finally, all patient volumes were then standardized to 224x224x25 volumetric data cubes for dimensional consistency.

The 34-layer pre-trained volumetric residual convolutional neural network framework from MONAI was used to obtain deep radiomic features. The weights from MONAI were obtained from training on eight different 3D MRI and CT segmentation datasets [56]. The radiomic features were subsequently inputted into a fully-connected neural network predictor, designed to classify breast cancer into no pCR or pCR.

For training, a learning rate of 0.001 was also used. All the model layers were trained with no freezing and leave-one-out cross-validation was used to compare the performance. Though the previous paper only reported the average accuracy, we also provide the average sensitivity, specificity, and F1 score.

Table 7.1 shows the results from using the unoptimized and optimized CDI^s with DWI to create a multiparametric MRI. As shown, the accuracy using the optimized CDI^s was 93.28%, over 5.5% higher than that previously reported (87.75%). Though the sensitivity and specificity metrics were not previously reported, using optimized CDI^s achieved over 90% for both sensitivity and specificity. Notably the F1 score using optimized CDI^s was also high at 90.17%. An example highlighting the visual differences between the imaging modalities of the unoptimized CDI^s and optimized CDI^s are shown in Figure 7.1. Also provided in Figure 7.1 are the associated tumour mask and DWI for the specific patient slice.

Table 7.1: Results using mpMRI^{cdis} with unoptimized and optimized CDI^s with the best result bolded.

mpMRI^{cdis} Version	**Accuracy**	**Sensitivity**	**Specificity**	**F1 score**
Unoptimized CDI^s	87.75%	N/A	N/A	N/A
Optimized PCa (ADC)	91.30%	93.90%	90.06%	87.50%
Optimized PCa (DWI)	32.81%	100.00%	0.58%	49.10%
Optimized BCa (ADC)	**93.28%**	**95.12%**	**92.40%**	**90.17%**
Optimized BCa (DWI)	82.21%	97.56%	74.85%	78.05%

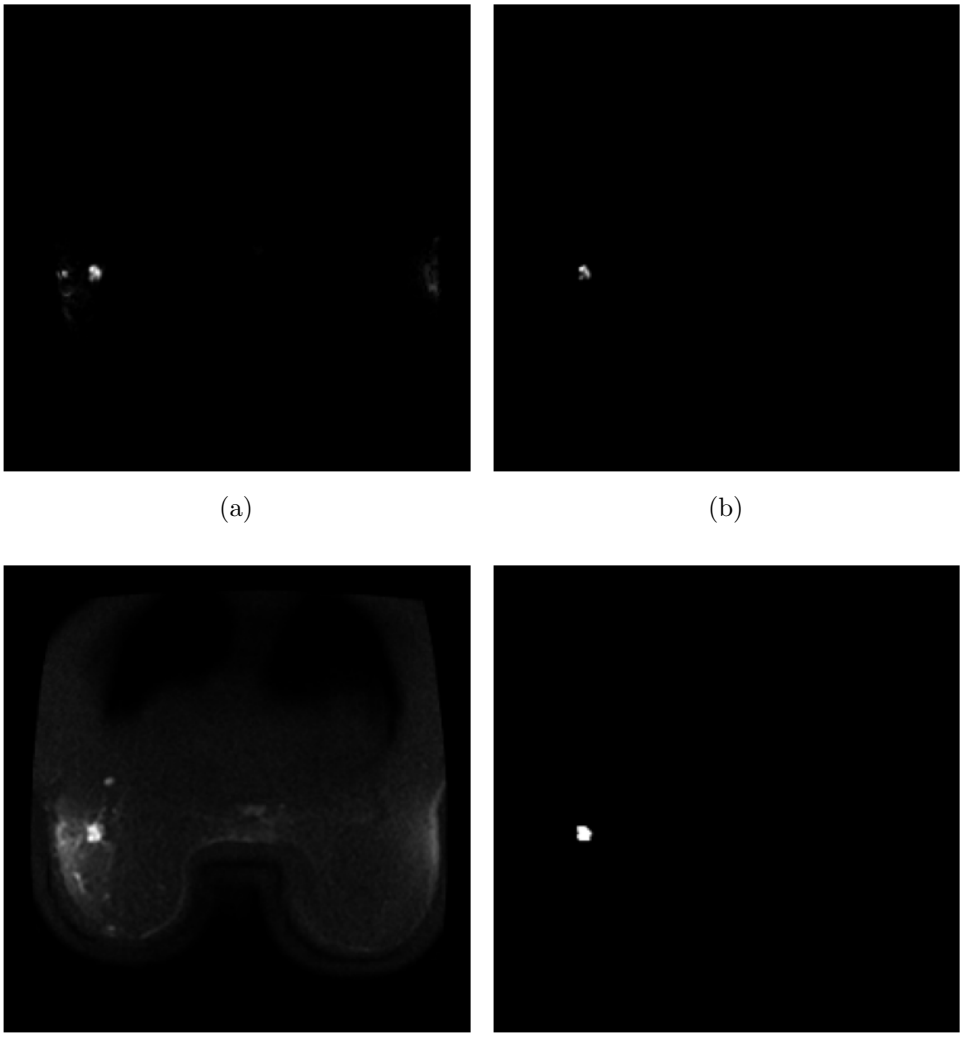

(a) (b)

(c) (d)

Figure 7.1: An example slice illustrating visual differences between (a) Unoptimized CDI^s, (b) Optimized CDI^s, (c) the associated DWI image, and (d) the associated tumour mask at pre-treatment for a patient who obtained pCR. For this patient, the pCR prediction was correct using the optimized CDI^s signal fused with DWI.

Table 7.2: SBR grade distribution in the patient cohort.

SBR Grade	Number of Patients
Grade I (Low)	10
Grade II (Intermediate)	99
Grade III (High)	200

7.3 Scarff-Bloom-Richardson Grade Classification

The data used in this study was the ACRIN study filtered for non-null SBR grade values, with a total of 309 patients remaining. Similar to Chapter 5, SBR grade I and II were combined into one category due to the imbalanced distribution between the three grades (as shown in Table 7.2).

The optimized CDI^s signals from Chapter 6 were fused with DWI to create a multiparametric MRI. To achieve dimensional consistency for machine learning, all volumes were then standardized into 224x224x25 volumetric data cubes for each patient.

The workflow used is the previously introduced deep radiomic clinical support workflow from Chapter 1. The pretrained 34-layer volumetric residual convolutional neural network architecture was initialized with the weights from MONAI [55] which were derived by training on the extensive 3D medical dataset, 3DSeg-8. This comprehensive dataset comprises images from eight different 3D segmentation datasets, encompassing both MRI and CT images [56]. The neural network is trained to extract deep radiomic features features which are then fed into a fully-connected neural network grade predictor to predict breast cancer grade (Grade I/Grade II and Grade III).

For training, a learning rate of 0.001 was used along with a weighted random sampler, AdamW optimizer, cross-entropy loss function and cosine annealing learning rate scheduler. All the model layers were also trained with no freezing. Leave-one-out cross-validation was conducted to obtain the results with the average accuracy, sensitivity, and specificity recorded.

As seen in Table 7.3, using the optimized CDI^s obtained a leave-one-out cross-validation of 95.79%, over 8% higher than that previously reported (87.70%). Optimizing CDI^s also achieved higher sensitivity and specificity, with all values above 90%. Figure 7.2 shows an illustrative example highlighting the visual differences between an unoptimized CDI^s signal and an optimized CDI^s signal, along with the corresponding tumour mask and DWI.

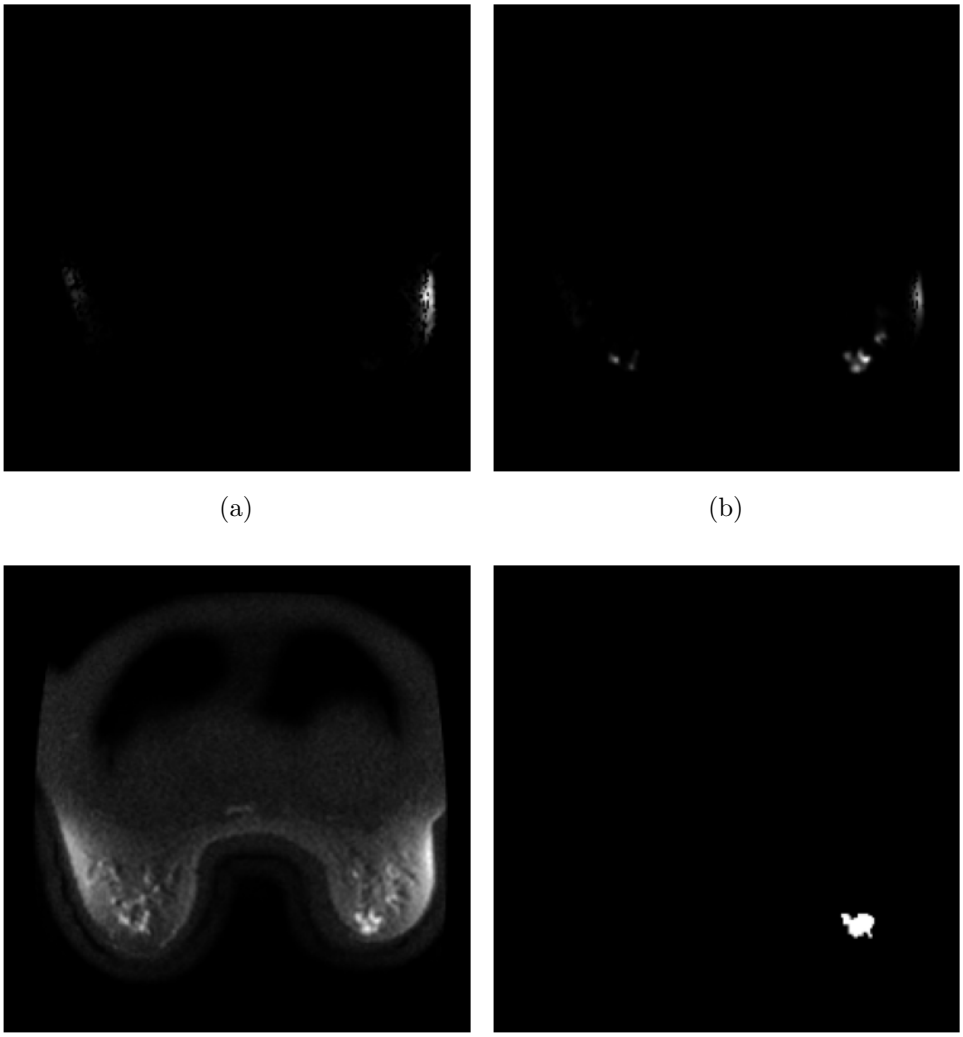

(a) (b)

(c) (d)

Figure 7.2: An example slice illustrating visual differences between (a) Unoptimized CDI^s, (b) Optimized CDI^s, (c) the associated DWI, and (d) the associated tumour mask for a patient who has SBR Grade III (High). In this patient case, grade prediction was correct using the optimized CDI^s signal fused with DWI.

Table 7.3: Results using mpMRI^{cdis} with unoptimized and optimized CDI^{s} with the best results bolded.

mpMRI^{cdis} Version	**Accuracy**	**Sensitivity**	**Specificity**	**F1 score**
Unoptimized CDI^{s}	87.70%	90.29%	81.82%	N/A
Optimized PCa (ADC)	90.61%	87.00%	97.25%	92.31%
Optimized PCa (DWI)	**95.79%**	**96.50%**	**94.50%**	**96.74%**
Optimized BCa (ADC)	64.72%	100.00%	0.00%	78.59%
Optimized BCa (DWI)	64.72%	100.00%	0.00%	78.59%

7.4 Summary

Given these promising results, the proposed noninvasive method that predicts pCR and classifies SBR grade would enhance patient treatment with minimal side effects (as it uses MRI modalities that are normally obtained in the course of the diagnosis). These results also highlight the importance of tuning CDI^{s} for the specific cancer domain as the optimized CDI^{s} modality obtains superior performance compared to unoptimized CDI^{s}.

Chapter 8

Conclusion

This chapter presents a summary of the thesis and contributions in Section 8.1 with the limitations and future work discussed in Section 8.2 and Section 8.3, respectively.

8.1 Summary of Thesis

In this thesis, the exploration and design of novel deep learning architectures for breast cancer was conducted to enhance two important breast cancer clinical tasks: pathologic complete response (pCR) prediction and Scarff-Bloom-Richardson (SBR) grade classification using a newly introduced MRI modality, CDI^s. Using a volumetric convolutional neural network architecture to learn volumetric deep radiomic features with a predictor that leverages the learned features, a proposed workflow is designed for pCR prediction and SBR grade classification. Further, the computation and optimization of CDI^s for improving breast cancer clinical task performance is also studied in this thesis.

The performance with optimized ($mpMRI^{cdis}$) is compared with the unoptimized $mpMRI^{cdis}$ and the current gold-standard MRI modalities (DWI, ADC, and T2w). Optimized $mpMRI^{cdis}$ was shown to achieve superior results over the current gold-standard MRI modalities and the unoptimized $mpMRI^{cdis}$. For grade prediction, using optimized CDI^s achieved a leave-one-out cross-validation accuracy of 95.79%, which is over 16% above the next best gold-standard MRI modality and over 6% above using the unoptimized CDI^s. Additionally, using optimized CDI^s for post-treatment response prediction resulted in a leave-one-out cross-validation accuracy of 93.28%, which is over 8.5% above the next best gold-standard MRI modality and over 5.5% above using the unoptimized

CDI^s. This improvement would greatly reduce overtreatment and ensure that patients who could substantially benefit from this treatment approach receive the care they need.

This thesis highlights the importance of leveraging CDI^s for cancer clinical tasks and tuning the parameters for the specific cancer domain. The proposed approach demonstrates how using optimized CDI^s can be used to enhance the performance of breast cancer clinical tasks, indicating its potential as a valuable tool for oncologists to enhance patient treatment within the breast cancer domain and beyond.

8.2 Limitations

Although these results are promising, the optimization of CDI^s was conducted using basic threshold-derived breast masks from the DWI images and were not verified by experienced radiologists. Moreover, the performance improvement of CDI^s over the best gold-standard imaging modality is marginal and could differ for another dataset. Though the Nelder-Mead optimization strategy is widely used, there is still the possibility that the chosen optimization coefficients were not globally optimal and there exists better coefficients which could be used. Lastly, since tumour masks were not provided for T2w images, the AUC performance could not be computed for the T2w modality, another gold-standard imaging modality, which may be able to better separate healthy and tumour tissue for breast.

8.3 Future Work

8.3.1 Breast Cancer Task Improvement

To further improve results, future work includes trying different feature extractors in the proposed clinical support workflow such as ResNet with more or less layers and new networks such as EfficientNet [64] or AttendNext [65]. Multimodal methods that combine both visual information (images) and textual information (patient metadata) should also be investigated further to further improve results.

8.3.2 Optimization Strategy Enhancement

This thesis primarily used the Nelder-Mead optimization strategy with the objective of tumour delineation. The optimization of the coefficients were conducted separately from

the training of the feature extractor. However, future work could examine combining the optimization with the training to generate better coefficients for the specific clinical task and hence, increase the performance on the particular clinical task.

8.3.3 Application to Other Domains

Another area of exploration is the application of CDI^s for other cancer domains, such as brain cancer, to enhance clinical support. In addition, even though Wong et al. explores computing and optimizing CDI^s for prostate cancer [10], there is a gap in analyzing the impact of using CDI^s for specific clinical tasks in prostate cancer such as predicting clinical significance from a patient's MRI.

References

[1] C.-e. A. Tai, H. Gunraj, and A. Wong, "A multi-institutional open-source benchmark dataset for breast cancer clinical decision support using synthetic correlated diffusion imaging data," *arXiv preprint arXiv:2304.05623*, 2023.

[2] C.-e. A. Tai, H. Gunraj, N. Hodzic, N. Flanagan, A. Sabri, and A. Wong, "Enhancing clinical support for breast cancer with deep learning models using synthetic correlated diffusion imaging," in *International Workshop on Applications of Medical AI*, pp. 83–93, Springer, 2023.

[3] Cancer.NET, "Breast cancer - statistics." https://www.cancer.net/cancer-types/breast-cancer/statistics, 2023. Accessed : 2023-06-10.

[4] D. Wang and et al., "Deep learning for identifying metastatic breast cancer," 2016.

[5] American Cancer Society, "Breast cancer." https://www.cancer.org/cancer/breast-cancer, 2022. Accessed: 2023-08-03.

[6] R. M. Mann, N. Cho, and L. Moy, "Breast mri: state of the art," *Radiology*, vol. 292, no. 3, pp. 520–536, 2019.

[7] E. Martinez-Heras and et al., "Diffusion-weighted imaging: Recent advances and applications," *Seminars in Ultrasound, CT and MRI*, vol. 42, no. 5, pp. 490–506, 2021. Advances in Neuroradiology I.

[8] A. Surov and et al., "Can diffusion-weighted imaging predict tumor grade and expression of ki-67 in breast cancer? a multicenter analysis," *Breast Cancer Research*, vol. 20, no. 58, 2018.

[9] D. Kawahara and Y. Nagata, "T1-weighted and t2-weighted mri image synthesis with convolutional generative adversarial networks," *Reports of Practical Oncology and Radiotherapy*, vol. 26, no. 1, pp. 35 – 42, 2021.

[10] A. Wong and et al., "Synthetic correlated diffusion imaging hyperintensity delineates clinically significant prostate cancer," *Scientific Reports*, vol. 12, no. 3376, 2022.

[11] N. C. Institute, "Tumor grade." https://www.cancer.gov/about-cancer/diagnosis-staging/diagnosis/tumor-grade, 2024. Accessed : 2024-03-19.

[12] Canadian Cancer Society, "Grading breast cancer." https://cancer.ca/en/cancer-information/cancer-types/breast/grading. Accessed: 2022-12-10.

[13] Cancer Research UK, "About breast cancer staging and grades." https://www.cancerresearchuk.org/about-cancer/breast-cancer/stages-grades/about. Accessed: 2024-03-19.

[14] American Cancer Society, "Breast cancer grade." https://www.cancer.org/cancer/types/breast-cancer/understanding-a-breast-cancer-diagnosis/breast-cancer-grades.html, 2024. Accessed: 2024-03-19.

[15] Canadian Cancer Society, "Prognosis and survival for breast cancer." https://cancer.ca/en/cancer-information/cancer-types/breast/prognosis-and-survival. Accessed: 2024-03-19.

[16] C. van Dooijeweert and et al., "Grading of invasive breast carcinoma: the way forward," *Virchows Archiv*, vol. 480, pp. 33–43, 2022.

[17] S. Amat and et al., "Scarff-bloom-richardson (sbr) grading: a pleiotropic marker of chemosensitivity in invasive ductal breast carcinomas treated by neoadjuvant chemotherapy," *Int J Oncology*, vol. 4, pp. 791–6, 2002.

[18] A. Conti and et al., "Radiomics in breast cancer classification and prediction," *Seminars in Cancer Biology*, vol. 72, pp. 238–250, 2021. Precision Medicine in Breast Cancer.

[19] J. R. Grajo and R. G. Barr, "Strain elastography for prediction of breast cancer tumor grades," *Journal of Ultrasound in Medicine*, vol. 35, no. 1, 2014.

[20] M. Fan and et al., "Joint prediction of breast cancer histological grade and ki-67 expression level based on dce-mri and dwi radiomics," *IEEE Journal of Biomedical and Health Informatics*, vol. 24, no. 6, pp. 1632–1642, 2020.

[21] H. D. Couture and et al., "Image analysis with deep learning to predict breast cancer grade, er status, histologic subtype, and intrinsic subtypes," *npj Breast Cancer*, vol. 4, no. 30, 2018.

[22] E. S. Burnside and et al., "Using computer-extracted image phenotypes from tumors on breast magnetic resonance imaging to predict breast cancer pathologic stage," *ACS Journals*, vol. 122, no. 5, pp. 748–757, 2016.

[23] C. Dimitrakakis and A. Keramopoulos, "Survival in primary inoperable breast cancer patients," *European Journal of Gynaecological Oncology*, vol. 25, no. 3, pp. 367–372, 2004.

[24] Jamie DePolo, "Pathologic complete response to targeted therapy before surgery linked to better survival for early-stage her2-positive breast cancer." https://www.breastcancer.org/research-news/neoadjuvant-pcr-linked-to-better-survival, 2020. Accessed: 2022-06-02.

[25] N. Kunst and et al., "Cost-effectiveness of neoadjuvant-adjuvant treatment strategies for women with erbb2 (her2)–positive breast cancer," *JAMA Network Open*, vol. 3, no. 11, 2020.

[26] S. Masood, "Neoadjuvant chemotherapy in breast cancers," *Womens Health*, vol. 12, no. 5, pp. 480–491, 2016.

[27] D. A. Redelmeier and et al., "Problems for clinical judgement: introducing cognitive psychology as one more basic science," *Canadian Medical Association Journal*, vol. 164, no. 3, pp. 358–360, 2001.

[28] H. J. Shin and et al., "Prediction of pathologic response to neoadjuvant chemotherapy in patients with breast cancer using diffusion-weighted imaging and mrs," *NMR Biomedical*, vol. 25, no. 12, pp. 1349–1359, 2012.

[29] X. B. Li and et al., "Biomarkers predicting pathologic complete response to neoadjuvant chemotherapy in breast cancer," *American Journal of Clinical Pathology*, vol. 145, no. 6, pp. 871–878, 2016.

[30] A. Fangberget and et al., "Neoadjuvant chemotherapy in breast cancer-response evaluation and prediction of response to treatment using dynamic contrast-enhanced and diffusion-weighted mr imaging," *European Radiology*, vol. 21, pp. 1188–1199, 2011.

[31] H. Moghadas-Dastjerdi and et al., "Machine learning-based a priori chemotherapy response prediction in breast cancer patients using textural ct biomarkers," in *42nd Annual International Conference of the IEEE Engineering in Medicine & Biology Society (EMBC)*, EMBC, (Montreal, QC, Canada), IEEE, 2020.

[32] H. Moghadas-Dastjerdi and et al., "A priori prediction of tumour response to neoadjuvant chemotherapy in breast cancer patients using quantitative ct and machine learning," *Scientific Reports*, vol. 10, pp. 1188–1199, 2020.

[33] R. Ha and et al., "Predicting post neoadjuvant axillary response using a novel convolutional neural network algorithm," *Annals of Surgical Oncology*, vol. 25, pp. 3037–3043, 2018.

[34] A. U. Haq and et al., "3dcnn: Three-layers deep convolutional neural network architecture for breast cancer detection using clinical image data," in *17th International Computer Conference on Wavelet Active Media Technology and Information Processing (ICCWAMTIP)*, ICCWAMTIP, (Chengdu, China), IEEE, 2020.

[35] H. Duanmu and et al., "Prediction of pathological complete response to neoadjuvant chemotherapy in breast cancer using deep learning with integrative imaging, molecular and demographic data," in *Medical Image Computing and Computer Assisted Intervention – MICCAI 2020* (A. L. Martel and et al., eds.), MICCAI, (Cham), pp. 242–252, Springer International Publishing, 2020.

[36] S. C. Partridge and et al., "Diffusion-weighted mri findings predict pathologic response in neoadjuvant treatment of breast cancer: The acrin 6698 multicenter trial," *Radiology*, vol. 289, no. 3, pp. 618–627, 2018.

[37] D. C. Newitt and et al., "Test–retest repeatability and reproducibility of adc measures by breast dwi: Results from the acrin 6698 trial," *Journal of Magnetic Resonance Imaging*, vol. 49, no. 6, pp. 1617–1628, 2018.

[38] D. C. Newitt and et al., "Acrin 6698/i-spy2 breast dwi [data set]," *The Cancer Imaging Archive*, 2021.

[39] K. Clark and et al., "The cancer imaging archive (tcia): Maintaining and operating a public information repository," *Journal of Digital Imaging*, vol. 26, no. 6, pp. 1045–1057, 2013.

[40] C. Westbrook and J. Talbot, *MRI in Practice*. John Wiley & Sons, 2018.

[41] R. H. Hashemi, W. G. Bradley, and C. J. Lisanti, *MRI: the basics: The Basics*. Lippincott Williams & Wilkins, 2012.

[42] G. Katti, S. A. Ara, and A. Shireen, "Magnetic resonance imaging (mri)–a review," *International journal of dental clinics*, vol. 3, no. 1, pp. 65–70, 2011.

[43] A. Qayyum, "Diffusion-weighted imaging in the abdomen and pelvis: concepts and applications," *Radiographics*, vol. 29, no. 6, pp. 1797–1810, 2009.

[44] S. Topics, "Diffusion weighted imaging - an overview." https://www.sciencedirect.com/topics/nursing-and-health-professions/diffusion-weighted-imaging, 2022. Accessed : 2022-07-15.

[45] L. C. Maas and P. Mukherjee, "Diffusion mri: overview and clinical applications in neuroradiology.," *Applied radiology*, vol. 34, no. 11, 2005.

[46] D. Le Bihan, "Looking into the functional architecture of the brain with diffusion mri," *Nature reviews neuroscience*, vol. 4, no. 6, pp. 469–480, 2003.

[47] R. Bammer, "Basic principles of diffusion-weighted imaging," *European journal of radiology*, vol. 45, no. 3, pp. 169–184, 2003.

[48] T. Henzler, P. Goldstraw, F. Wenz, R. Pirker, W. Weder, P. Apfaltrer, M. Meyer, K. Buesing, L. Crino, D. Fennell, *et al.*, "Perspectives of novel imaging techniques for staging, therapy response assessment, and monitoring of surveillance in lung cancer: Summary of the dresden 2013 post wclc-iaslc state-of-the-art imaging workshop," *Journal of Thoracic Oncology*, vol. 10, no. 2, pp. 237–249, 2015.

[49] G. B. Chavhan, P. S. Babyn, B. Thomas, M. M. Shroff, and E. M. Haacke, "Principles, techniques, and applications of t2*-based mr imaging and its special applications," *Radiographics*, vol. 29, no. 5, pp. 1433–1449, 2009.

[50] W. A. Gibby, "Basic principles of magnetic resonance imaging," *Neurosurgery Clinics*, vol. 16, no. 1, pp. 1–64, 2005.

[51] E. A. Walker, M. E. Fenton, J. S. Salesky, and M. D. Murphey, "Magnetic resonance imaging of benign soft tissue neoplasms in adults," *Radiologic Clinics*, vol. 49, no. 6, pp. 1197–1217, 2011.

[52] Y. Chen, S. J. Almarzouqi, M. L. Morgan, and A. G. Lee, *T2-Weighted Image*, pp. 1750–1752. Vol. 1 of Schmidt-Erfurth and Kohnen [66], 2018.

[53] A. Wong, J. Glaister, A. Cameron, and M. Haider, "Correlated diffusion imaging," *BMC medical imaging*, vol. 13, pp. 1–7, 2013.

[54] K. He, X. Zhang, S. Ren, and J. Sun, "Deep residual learning for image recognition," in *Proceedings of the IEEE conference on computer vision and pattern recognition*, pp. 770–778, 2016.

[55] M. Consortium, "Project monai." https://docs.monai.io/en/stable/index.html#, 2024. Accessed : 2024-02-25.

[56] S. Chen, K. Ma, and Y. Zheng, "Med3d: Transfer learning for 3d medical image analysis," *arXiv preprint arXiv:1904.00625*, 2019.

[57] M. A. Marino, T. Helbich, P. Baltzer, and K. Pinker-Domenig, "Multiparametric mri of the breast: A review," *Journal of Magnetic Resonance Imaging*, vol. 47, no. 2, pp. 301–315, 2018.

[58] Q. Hu, H. M. Whitney, and M. L. Giger, "A deep learning methodology for improved breast cancer diagnosis using multiparametric mri," *Scientific reports*, vol. 10, no. 1, p. 10536, 2020.

[59] K. Hara, H. Kataoka, and Y. Satoh, "Learning spatio-temporal features with 3d residual networks for action recognition," *CoRR*, vol. abs/1708.07632, 2017.

[60] Valley County Health System, "How painful is breast cancer biopsy & how long does it take to recover." https://www.valleycountyhealthsystem.org/about-us/news-events/blog/how-painful-is-breast-cancer-biopsy-and-how-long-does-it-take-to-recover.html, 2020. Accessed: 2022-12-10.

[61] MDsave, "Breast biopsy." https://www.mdsave.com/procedures/breast-biopsy/d78af5cf. Accessed: 2022-12-14.

[62] R. Parikh, A. Mathai, S. Parikh, G. C. Sekhar, and R. Thomas, "Understanding and using sensitivity, specificity and predictive values," *Indian journal of ophthalmology*, vol. 56, no. 1, pp. 45–50, 2008.

[63] J. A. Nelder and R. Mead, "A simplex method for function minimization," *The computer journal*, vol. 7, no. 4, pp. 308–313, 1965.

[64] M. Tan and Q. Le, "Efficientnet: Rethinking model scaling for convolutional neural networks," in *International conference on machine learning*, pp. 6105–6114, PMLR, 2019.

[65] A. Wong, M. J. Shafiee, S. Abbasi, S. Nair, and M. Famouri, "Faster attention is what you need: a fast self-attention neural network backbone architecture for the edge via double-condensing attention condensers," *arXiv preprint arXiv:2208.06980*, 2022.

[66] U. M. Schmidt-Erfurth and T. Kohnen, eds., *Encyclopedia of ophthalmology.* 1, Springer,, 2019.